A high-resolution, quantitative, rainfall record of the last 1000 years in the Australian sub-tropics

Thesis submitted in accordance with the requirements of the University of Adelaide for an Honours Degree in Geology

Julian Steele Greer

November 2015

THE UNIVERSITY of ADELAIDE

A HIGH-RESOLUTION, QUANTITATIVE, RAINFALL RECORD OF THE LAST 1000 YEARS IN THE AUSTRALIAN SUB-TROPICS.

LATE-HOLOCENE RAINFALL IN SE QUEENSLAND

ABSTRACT

Knowledge on the behaviour of the El Niño–Southern Oscillation (ENSO) over the past millennium has been composed of proxy records collected across the Southern Hemisphere but conflicting patterns often emerge. Few western Pacific ENSO records exist covering this timeframe, even less focus on the effect of ENSO on Australian climate. To develop a quantitative late-Holocene climate record for sub-tropical Australia, leaf fragments of *Melaleuca quinquenervia* were extracted from a sediment core from Swallow Lagoon, North Stradbroke Island, south-east Queensland. The sub-fossil leaves were isolated from lake sediments under a microscope. AMS ^{14}C-dating was performed and an age-depth model covering 514-2013 common era (CE) was developed. Carbon isotope ratios ($\delta^{13}C$) of bulk leaf tissue were measured and carbon isotope discrimination (Δ) was calculated. A previously developed equation (Tibby et al. in review) based on the relationship between modern *M. quinquenervia* Δ and rainfall was used to reconstruct late-Holocene rainfall. Reconstructed rainfall was compared to historical records from the region. When individual samples were compared to instrumental records, there was no observable relationship between Δ and rainfall. However, multi-decadal shifts in climate seen in the historical record were reproduced by the proxy reconstruction, with the mean reconstructed rainfall falling within the 1σ range of the instrumental data. The rainfall reconstruction for the late-Holocene was then examined to assess shifts in climate state across multi-decade scale climate phases including the Medieval Climate Anomaly (MCA) and the Little Ice Age (LIA). The median rainfall during the MCA was found to be similar to that of the LIA (1663 mm and 1654 mm respectively), while the historical period was significantly drier (1236 mm). The results of this study characterize ENSO conditions in Australia as La Niña-dominated during the LIA and MCA. The historical period, by contrast, was more El Niño-dominated than any other period.

KEYWORDS

Geochemistry, Carbon Isotope ratio, *Melaleuca quinquenervia*, Holocene, Precipitation, El Niño Southern Oscillation

TABLE OF CONTENTS

LIST OF FIGURES

LIST OF TABLES

INTRODUCTION

The El Niño–Southern Oscillation

The El Niño–Southern Oscillation (ENSO) influences climate variability on an annual to millennial scale across over half of the globe (Tudhope et al. 1995; Cobb et al. 2003; Chiang 2009; Koutavas and Joanides 2012; Liu et al. 2014). While some aspects of the physics driving ENSO are well understood, the variability in the frequency and strength of ENSO events, as well as how the ENSO system responds to changes in climate, such as those projected for the 21st Century, are still poorly understood (Tudhope et al. 2001; Liu 2012). To resolve these uncertainties, palaeoclimatological data can be used to better understand the behaviour of the ENSO system over time (Emile-Geay et al. 2013).

The Southern Oscillation refers to a seesaw in atmospheric pressure between the central and west Pacific, typically with a 2-7 yearr period (Tudhope et al. 1995; Chiew et al. 1998; Mann et al. 2005). When sea surface temperature (SST) and atmospheric pressure in the central Pacific region are higher than those in the western Pacific, the Southern Oscillation is said to be in an El Niño phase. When there is higher SST and atmospheric pressure in the western Pacific, the Southern Oscillation is said to be in a La Niña phase (Tudhope et al. 1995). Although ENSO is controlled by ocean circulation and pressure regimes in the Pacific Ocean, atmospheric teleconnections link the inter-annual climate variability caused by ENSO to climatic anomalies throughout the globe (Tudhope et al. 1995; Chiew et al. 1998; Vance et al. 2013).

ENSO causes marked variations in the hydrological cycle on seasonal and annual scales due to sub-decadal SST fluctuations in the western Pacific (Chiew et al. 1998; Chen et al. 2004; Zebiak et al. 2015). On an inter-decadal scale, ENSO variability is driven by variability in Pacific SST. In addition, there is also a multi-decadal pattern in SST variability, which acts on a 50–70 year time scale (Liu 2012). ENSO variance is not just an oscillation between El Niño and La Niña events; the system can have many El Niño events in succession, creating an average El Niño-like climate state, or many La Niña events leading to an average La Niña-like state (Diaz et al. 2001; Cobb et al. 2013). Extreme El Niño or La Niña phases can cause climate variations over longer timescales by shifting the average climate state (Cane 2005). Palaeoclimate data are particularly useful at documenting these shifts in climate state and multi-decadal ENSO variability (Vance et al. 2013).

Regional Expressions of ENSO

Sub-tropical Australia experienced predominantly dry conditions during the early Holocene, before the establishment of the modern ENSO system (Donders et al. 2006). The onset of the modern ENSO system began around 6 ka cal BP and brought significant precipitation variability to the region (Rodbell et al. 1999; Donders et al. 2007; Cobb et al. 2013; Dassié et al. 2014; Liu et al. 2014). Evidence from storm-induced lake laminae in Ecuador, tied to historic El Niño activity, shows there has been a progressive increase in the frequency of El Niño events from the mid-Holocene (Moy et al 2002). Today, above average rainfall in eastern Australia is associated with the La Niña phase of the Southern Oscillation, while the El Niño phase brings drier conditions (Chiew et al. 1998). For example, the pronounced flooding of south-east Queensland in

January 2011 was associated with a strong La Niña phase (Bureau of Meteorolgy 2015a).

The climate in sub-tropical Australia is widely believed to have been much more variable in the late-Holocene under the influence of ENSO, than it was during the early-Holocene (Donders et al. 2006; Petherick et al. 2008). However, the data are limited to a small number of sites where the records may be confounded by other factors such as increased moisture availability due to sea level rise (Donders et al. 2006). In contrast to the evidence from eastern Australia, more recent evidence from the central Pacific suggests that there was no mid-Holocene intensification of ENSO (Cobb et al. 2013). To improve the understanding of how ENSO variability responds to external climate forcing, its past variability must be studied further (Cobb et al. 2013; Liu et al. 2014). Unfortunately, due to the limited and often conflicting nature of Southern Hemisphere palaeoclimate records, investigating past ENSO variability is a challenging task (Goodwin et al. 2014).

The Medieval Climate Anomaly (MCA) (900-1250 CE) and the Little Ice Age (LIA) (1500-1850 CE) are two important climate phases which have been intensively studied to examine ENSO behaviour over the past millennium. The transition between these phases represents a prominent shift in global climate under boundary conditions similar to the present day (Wanner et al. 2008). During the MCA, many Southern Hemisphere records show a shift in average ENSO conditions to more La Niña-dominated (Goodwin et al. 2014), while others suggest more El Niño-dominated climate (Neukom et al. 2011; Emile-Geay et al. 2013; Vance et al. 2013). A consensus is hard to attain due to reliance

on sparse proxy records and the added effects of regional variables (Table 1). At the onset of the MCA, ca. 900-950 CE, there is evidence from fossil coral oxygen-18 signatures ($\delta^{18}O$) that the climate in the tropical Pacific was predominantly cool and dry (Cobb et al. 2003; Allen 2006). Cool, dry conditions across the Pacific are associated with a suppressed ENSO system, expressing a La Niña phase (Ropelewski and Halpert 1989; Mason and Goddard 2001). These La Niña conditions are also thought to have occurred from 1150-1250 CE, with models based on the coral record predicting very few El Niño events (Cane 2005). In contrast, summer sea salts preserved in Law Dome, Antarctica that are derived from eastern Australia suggest Australia experienced an El Niño-dominated climate across this same interval, from 1000-1260 CE (Vance et al. 2013).

Table 1: Palaeoclimate studies used to determine ENSO state during the Medieval Climate Anomaly (MCA) ordered E-W by study region.

Region	Proxy	Record	MCA Climate	Reference(s)
Central America	Speleothem $\delta^{18}O$	1850 BCE - 1779 CE	La Niña-dominated (860-1300 CE)	(Carrillo-Bastos et al. 2013)
Southern South America	Multi-proxy network	900-2000 CE	El Niño-dominated	(Neukom et al. 2011)
Peru	Glacial Ice $\delta^{18}O$	200-2000 CE	La Niña-dominated	(Thompson et al. 2013)
Pacific	ZC Model, multi-proxy network	1000-2000 CE	La Niña-dominated	(Mann et al. 2005)
Central Pacific	Coral $\delta^{18}O$	900-2000 CE	La Niña-dominated	(Cobb et al. 2003)
Central Pacific	Multi-proxy network	1000-2000 CE	El Niño-dominated	(Emile-Geay et al. 2013)
West Pacific	Foraminifera $\delta^{18}O$	168-1852 CE	La Niña-dominated	(Khider et al. 2011)
Australia	Antarctic ice core sea salt	1000-2009 CE	El Niño-dominated (1000-1260 CE)	(Vance et al. 2013)

During the LIA, fossil coral $\delta^{18}O$ from across the central Pacific suggest intense El Niño activity which would have driven an increase in precipitation, with stormy conditions more prevalent in that region (Cobb et al. 2003; Allen 2006). An El Niño dominated climate state is believed to have prevailed throughout the LIA, with numerous El Niño events in the proxy record (Cane 2005) (Table 2). Again, the Antarctic ice core records contrast the general consensus, suggesting a La Niña-dominated Australia from 1260-1860 (Vance et al. 2013). In a multi-proxy study, Emile-Geay et al. (2013) also found that the LIA was subject to a cooler eastern Pacific region and an overall La Niña-dominated climate.

Table 2: Palaeoclimate studies used to determine ENSO state during the Little Ice Age (LIA) ordered E-W by study region.

Region	Proxy	Record	LIA Climate	Reference(s)
Central America	Speleothem $\delta^{18}O$	1850 BCE-1779 CE	El Niño-dominated (1300-1760 CE)	(Carrillo-Bastos et al. 2013)
Southern South America	Multi-proxy network	900-2000 CE	La Niña-dominated	(Neukom et al. 2011)
Peru	Glacial Ice $\delta^{18}O$	200-2000 CE	El Niño-dominated (1520-1880 CE)	(Thompson et al. 2013)
Pacific	ZC Model, multi-proxy network	1000-2000 CE	El Niño-dominated	(Mann et al. 2005)
Central Pacific	Coral $\delta^{18}O$	900-2000 CE	El Niño-dominated	(Cobb et al. 2003)
Central Pacific	Multi-proxy network	1000-2000 CE	La Niña-dominated	(Emile-Geay et al. 2013)
Fiji	Coral $\delta^{18}O$	1617-2004 CE	El Niño-dominated	(Drassié et al. 2014)
South Pacific	Coral Sr/Ca	1726-1997 CE	El Niño-dominated (1726-1765 CE)	(Linsley et al. 2000)
New Zealand	Multi-proxy network and synoptic typing	1750-2005 CE	La Niña-dominated	(Lorrey et al. 2013)
West Pacific	Foraminifera $\delta^{18}O$	168-1852 CE	El Niño-dominated	(Khider et al. 2011)
Qld, Australia	Coral $\delta^{18}O$, Sr/Ca, U/Ca	1565-2000 CE	El Niño-dominated	(Hendy et al. 2002)
Qld, Australia	Coral luminescence	1639-2000 CE	El Niño-dominated	(Lough 2011)
Australia	Antarctic ice core sea salt	1000-2009 CE	La Niña-dominated (1260-1860 CE)	(Vance et al. 2013)

Over the historical period (1910-2015 CE), Vance et al. (2013) identified signatures indicative of El Niño activity in the sea salts preserved in Antarctic ice cores. Fijian fossil coral $\delta^{18}O$ records increased ENSO frequency into the historical period (Dassié et al. 2014), which has brought above average inter-annual variability, especially since 1900 (Chen et al. 2004). Cobb et al. (2013) suggests that high variability in the ENSO system in the historical period is not unprecedented; however, this period has seen numerous intense El Niño events. The El Niño events of 1982/83 and 1997/98 had particularly widespread ecological, social and economic impacts (Tudhope et al. 2001). The historical period is largely regarded to be El Niño-dominated (Table 3).

Table 3: Palaeoclimate studies used to determine ENSO state during the historical period ordered E-W by study region.

Region	Proxy	Record	Historical Climate	Reference(s)
Southern South America	Multi-proxy network	900-2000 CE	El Niño-dominated	(Neukom et al. 2011)
Peru	Glacial Ice $\delta^{18}O$	200-2000 CE	La Niña-dominated	(Thompson et al. 2013)
Pacific	ZC Model, multi-proxy network	1000-2000 CE	El Niño-dominated	(Mann et al. 2005)
Central Pacific	Coral $\delta^{18}O$	900-2000 CE	El Niño-dominated	(Cobb et al. 2003)
Central Pacific	Multi-proxy network	1000-2000 CE	El Niño-dominated	(Emile-Geay et al. 2013)
Fiji	Coral $\delta^{18}O$	1617-2004 CE	El Niño-dominated	(Drassié et al. 2014)
South Pacific	Coral Sr/Ca	1726-1997 CE	El Niño-dominated	(Linsley et al. 2000)
New Zealand	Multi-proxy network and synoptic typing	1750-2005 CE	El Niño-dominated	(Lorrey et al. 2013)
Qld, Australia	Coral $\delta^{18}O$, Sr/Ca, U/Ca	1565-2000 CE	El Niño-dominated	(Hendy et al. 2002)
Qld, Australia	Coral luminescence	1639-2000 CE	La Niña-dominated	(Lough 2011)
Australia	Antarctic ice core sea salt	1000-2009 CE	El Niño-dominated	(Vance et al. 2013)

These observed shifts between El Niño and La Niña dominated states could be explained by the ocean dynamical thermostat hypothesis (Clement et al. 1996). The ocean dynamical thermostat is a negative feedback in which warmer global conditions drive upwelling of cool water from depth in the eastern Pacific. This is believed to inhibit surface warming in the central and eastern Pacific, enhancing the east-west SST gradient, and creating La Niña conditions (Clement et al. 1996; Emile-Geay et al. 2013). The hypothesis states that given relatively high solar irradiance during the Medieval Climate Anomaly (MCA), the ocean dynamical thermostat would result in a greater east-west SST gradient driving a La Niña climate state (Emile-Geay et al. 2013). During the LIA, increased volcanic activity in the tropics (Mann et al. 2005) would drive warmer eastern Pacific SST and result in an El Niño climate state (Emile-Geay et al. 2013).

Due to the conflicting nature of palaeoclimate records described above, several records do not support the ocean dynamical thermostat hypothesis, such as recent work which found that the LIA was significantly wetter than the MCA (Vance et al. 2015). Other recent evidence suggests that solar forcing had little influence on ENSO variance during the late-Holocene (Cobb et al. 2013). It is crucial to test the validity of the ocean dynamical thermostat hypothesis by checking these conflicting claims as the way climate across the Pacific region responded to natural climate forcing in the past serves as an indication of its sensitivity to anthropogenic climate change (Emile-Geay et al. 2013).

As Eastern Australia's climate is highly sensitive to ENSO dynamics, an understanding of its Palaeoclimate can help resolve the debate around the behaviour of ENSO during the MCA and LIA. Unfortunately very few terrestrial palaeoclimate records exist to help characterize the climate over the past millennium. Australian climate has largely been inferred from records taken from locations distant from the Australian continent, such as Antarctica (Vance et al. 2013). A quantitative record of precipitation from terrestrial Australia would provide an important perspective, as the nature of the teleconnections between Australia and other localities may not be stable (Gallant et al. 2013).

Plants as Precipitation Proxies

Analysis of isotope values and their fractionation in plant tissue is an important technique for proxy reconstruction of palaeoenvironments (Barbour 2007). Physical and biological processes in plant leaves favour ^{12}C over ^{13}C via diffusion through stomata, and the enzymatic processes involved in photosynthesis (Marshall et al. 2007; Marshall et al. 2008). The carbon isotopic composition is reported as a $\delta^{13}C$ value, calculated as (Farquhar et al. 1982):

$$\delta^{13}C = (R_{sample} / R_{standard} - 1) \times 1000 \quad (1)$$

where R_{sample}, the ratio of $^{13}C/^{12}C$ in the sample is compared to $R_{standard}$, the $^{13}C/^{12}C$ ratio in the international standard, a Cretaceous belemnite from the Peedee formation in South Carolina, USA (Cernusak et al. 2008).

Carbon isotope discrimination (Δ) of plant tissue relative to CO_2 in the atmosphere is described using the following formula (Arens et al. 2000; Cernusak et al. 2013)

$$\Delta = (\delta^{13}C_{atmosphere} - \delta^{13}C_{plant}) / (1 + \delta^{13}C_{plant} / 1000) \quad (2)$$

where the $\delta^{13}C_{atmosphere}$ is the carbon isotope composition of atmospheric CO_2, and $\delta^{13}C_{plant}$ is the bulk carbon isotopic composition measured in plant tissue.

Carbon isotope discrimination (Δ) relative to the atmosphere can be modelled as (Farquhar et al. 1989):

$$\Delta = a + (b - a)\, c_i/c_a \quad (3)$$

where *a* represents fractionation due to diffusion across the stomatal boundary (4.4 ‰) and *b* represents fractionation caused by carboxylation (27 ‰). Discrimination is modulated by c_i/c_a which is the ratio of c_i, partial pressure of CO_2 (pCO_2) inside the leaf; and c_a, pCO_2 of the atmosphere (Farquhar et al. 1989).

Carbon isotope discrimination between bulk leaf and atmospheric carbon dioxide is lower when plants are suffering moisture stress associated with drier climates. This is because the plant's stomata are closed to prevent water loss, reducing the supply of CO_2 in the leaf. Provided photosynthesis continues, the demand for carbon remains unchanged (Farquhar et al. 1989; Cernusak et al. 2013). This causes the ratio c_i/c_a to approach a value of zero and Δ values to approach the value of *a*. In wetter climates, plant stomata are open and the plant is free to utilise ^{12}C from a relatively endless supply. Thus, c_i/c_a approaches a value of one and Δ values are closer to the value of *b* (Farquhar et al. 1989; Cernusak et al. 2013). The relationship between c_i/c_a and water stress is strongest when other potentially limiting factors, such as light availability, do not constrain photosynthesis (Diefendorf et al. 2010; Cernusak et al. 2013). Light limitation lowers the photosynthetic (and therefore CO_2) demand of the plant, resulting in higher c_i and a greater c_i/c_a ratio. In many sub-tropical vegetation communities, such

as the *Melaleuca quinquenervia* (Myrtaceae) community used in this study, light limitation is restricted to self-shading and light availability does not play a limiting role in discrimination (Tibby et al. in review; personal observation, 17 March 2015).

Several studies have shown that there is a negative linear correlation between the bulk $\delta^{13}C$ of C_3 plant material and mean annual precipitation (MAP) (Stewart et al. 1995; Diefendorf et al. 2010; Prentice et al. 2011). As increasing MAP causes more negative $\delta^{13}C$ values, these result in larger, more positive Δ values. In addition, as c_i/c_a is dependent on atmospheric pCO_2, a relationship can be established between Δ and pCO_2. This is described by the following hyperbolic formula (Schubert and Jahren 2012):

$$\Delta = [(28.26)\ (0.21)\ (pCO_2 + 25)] / [28.26 + (0.21)\ (pCO_2 + 25)] \qquad (4)$$

where 28.26 is the asymptotic limit to $\delta^{13}C$, 0.21 is a measure of responsiveness and 25 accounts for fractionation across the stomatal boundary such that $\Delta = 4.4$ ‰ at $pCO_2 = 0$ ppm. These are experimentally derived constants which fit the general form of the equation to C_3 plant species (Schubert and Jahren 2012).

Using the observed correlation between Δ and MAP, Tibby et al. (in review) developed a calibration based on the Δ values of modern *M. quinquenervia* leaves that can be applied to leaves preserved in the fossil record. Their model is based on the discrimination anomaly between the measured and predicted Δ values; where the "measured" Δ is calculated (Equation 3) from $\delta^{13}C$ observed in the leaves, and "predicted" Δ is based on pCO_2 (Equation 4). As most *M. quinquenervia* leaves remain on trees for 2 to 4 years in south-east Queensland, yearly Δ averages were derived and regressed against the average MAP for a number of years prior to leaf fall.

The best model achieved by the study was based on the relationship between average precipitation over the three years leading up to leaf collection and the discrimination anomaly. This relationship is described by the following formula (Tibby et al. in review):

$$MAP_{(3\ years)} = 214.82(\Delta_{calculated} - \Delta_{predicted}) + 819.42 \quad (5)$$

Study Location

North Stradbroke Island (NSI) covers 285 km^2, and sits on the eastern edge of Moreton Bay, south-east Queensland (Figure 1; Mosisch and Arthington 2001). With an average annual rainfall of 1587 mm and a mean annual maximum temperature of 25 °C, the climate on NSI is strongly influenced by ENSO (Barr 2012). The hydrology of the island is influenced by its two main land forms, both parabolic dunes and strand plains, which were both formed by wind-blown siliciclastic sediments during the late Pleistocene and Holocene (Petherick et al. 2009; Leach 2011; Moss et al. 2013). Amid the high sand dunes, Swallow Lagoon (S 27.49846, E 153.45500) sits isolated, independent from the regional water table with its volume and level entirely controlled by precipitation (Cox et al. 2011; Leach 2011). The lagoon features a deep accumulation of organic sediment overlying a base of fine sands. The organic sediments are predominately composed of *Lepironia articulata* (Cyperaceae), a sedge plant growing in the lagoon, *M. quinquenervia*, growing adjacent to the lagoon, and to a lesser extent, several eucalypt species from the surrounding woodland (Marshall and McGregor 2011; observation, 17 March 2015; Barr, pers. comm., 8 April 2015). *M. quinquenervia* leaves are present throughout the lake sediment record, with the species

having grown nearby to Swallow Lagoon for at least 7520 years (Barr and Tibby, pers. comm., 19 August 2014).

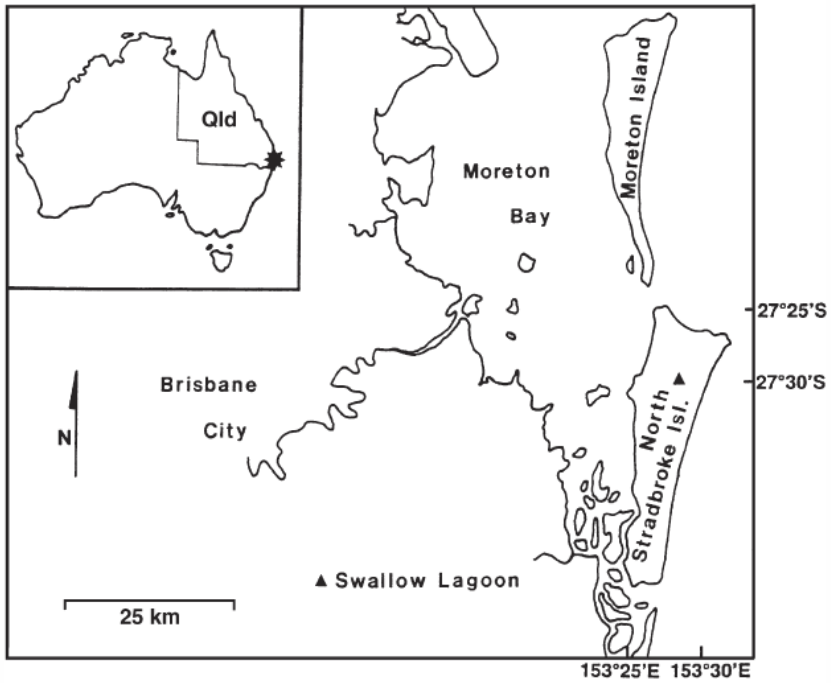

Figure 1: Map of Moreton Bay, south-east Queensland, showing the geographic location of North Stradbroke Island (triangle). Inset shows Australia, with Morton Bay marked by a black star (figure adapted from Mosisch and Arthington 2001).

Claims

This study will test whether the quantifiable relationships between bulk leaf $\delta^{13}C$ and rainfall records observed previously in modern *M. quinquenervia* leaves (Tibby et al. in review) are observable the carbon isotope values retrieved from sub-fossil *M. quinquenervia* preserved in lake sediments from the historic period. This test will serve as an internal validation of a rainfall reconstruction based on those modern relationships. The rainfall reconstruction will be used to tests the hypothesis that eastern Australia received high precipitation during the Medieval Climate Anomaly (MCA), under a La Niña-dominated climate state. It will also test whether an El Niño-dominated climate state resulted in lower precipitation during the Little Ice Age (LIA). The

hypothesis that the historical period has received lower levels of precipitation, due to a dominance of El Niño events, will also be tested. Testing these hypotheses will provide insight on ENSO dynamics throughout the past millennium and help further develop understanding around the influence of the ocean dynamical thermostat on ENSO patterns.

Agenda

In this thesis, an age-depth model covering the past 1.5 ka is established for a 91 cm sediment core collected from Swallow Lagoon in March 2015. The core features a very high concentration of leaves from the C_3 plant *M. quinquenervia.* Radiocarbon dating is based on 13 *M. quinquenervia* leaf samples collected from various depths within the core. The concentration of ^{14}C dates this represents means that this record is one of the best dated millennial-length sediment records in Australia (Hua, pers. comm., 17 August 2015). Such precision is necessary to properly assess the nature of climate variability during the short-lived Medieval Climate Anomaly, Little Ice Age and historical period.

Bulk leaf $\delta^{13}C$ data from the *M. quinquenervia* leaves collected in this study are used to calculate Δ using Equations 3 and 4 with historic and late-Holocene atmospheric $\delta^{13}C$ and pCO_2 records taken from GLOBALVIEW monitoring stations and Antarctic ice core records (Etheridge et al. 1996; Francey et al. 1999; Monnin et al. 2004; Elsig et al. 2009; GLOBALVIEW-CO2C13 2013). Birks (1998) emphasises that testing relationships established in the historical period with measured historical data is the best test of the validity of proxy-environment calibrations, yet this is rarely carried out due to a lack of historical data, adequate proxy data coverage of the historical period or both

(Tibby, pers. comm., 22 September 2015). This study employs measurements of leaf Δ from the most recent 100 years of the core to test the established rainfall calibration based on modern day *M. quinquenervia* leaves collected over an 11-year period, nearby to NSI (Equation 5; Tibby et al. in review). Measurements from the remaining length of the core are used to create a rainfall reconstruction covering the LIA and MCA. This gives a western Pacific perspective on the late Holocene ENSO system and a sub-tropical Australian perspective on the controversy over which climate states were dominant over this time frame. In-so-doing this study provides the only high-resolution quantitative rainfall record covering the late Holocene in Australia.

METHODS

Leaf Preparation

Two sediment cores were taken from Swallow Lagoon (Figure 2). The 91 cm core, (SL-15/2) was chosen for study due to the continuous preservation of *M. quninquenervia* leaves throughout the record. The leaf-fragment yield of both SL-15/1 and SL-15/2 were assessed in the field, during the collection process.

The cores were extruded and sub-sampled at one centimetre resolution, on-site, immediately after coring, using a pallet knife and purpose-built collar, which fit over the core barrel. In the laboratory, the sediment samples were sieved to remove material <500 μm, which was collected in glass beakers and then stored in 120 mL plastic containers in a freezer set to -17°C. For the 20 basal samples (71-91 cm) the material remaining on the sieve was washed into a watch glass, where the *M. quninquenervia* leaf fragments could be picked out from material >500 μm under a stereoscope. For

shallower samples, where leaves were generally more intact and fragments larger, potential *M. quninquenervia* leaves could be identified and picked directly from the sieve. Leaves were then examined under the stereoscope for identification (Figure 2). All material >500 µm from samples handled in this manner was returned to the sample bags and frozen. Full methods relating to core extraction and sampling are included in Appendix A.

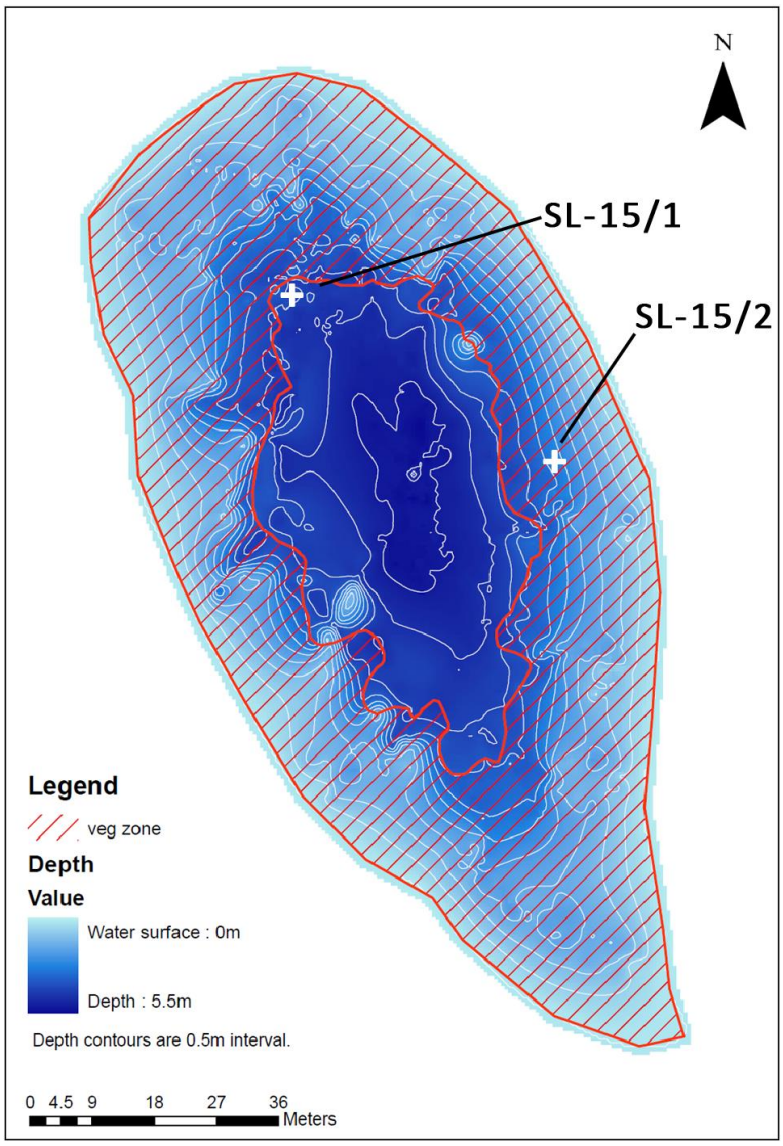

Figure 2: Bathymetric map of Swallow Lagoon, as surveyed in October 2009 with interpolated 1 m contour lines and hashed region representing the distribution of *Lepironia articulata* (figure adapted from Marshall and McGregor, 2011). Elevation at the water's edge is 152 m (Australian Height Datum, expressed in metres above mean sea level). 2015 core sites are indicated, this study focuses on data from core SL-15/2, taken from shallows on the eastern side of the lake.

Leaves were identified as *M. quninquenervia* based on their orange to reddish-brown colouration, thick stem with five veins running parallel to the leaf length, from which the epithet "quinquenervia" is derived, and the appearance of yellow oil glands between the veins, a diagnostic feature of Myrtaceae such as *Melaleuca* (Figure 3). The recovered leaves were placed into 50 mL polyethylene centrifuge tubes. The collected leaves and remaining material were stored in a freezer at -17°C before being placed in a freeze drier for 24-48 hours to remove all remaining moisture.

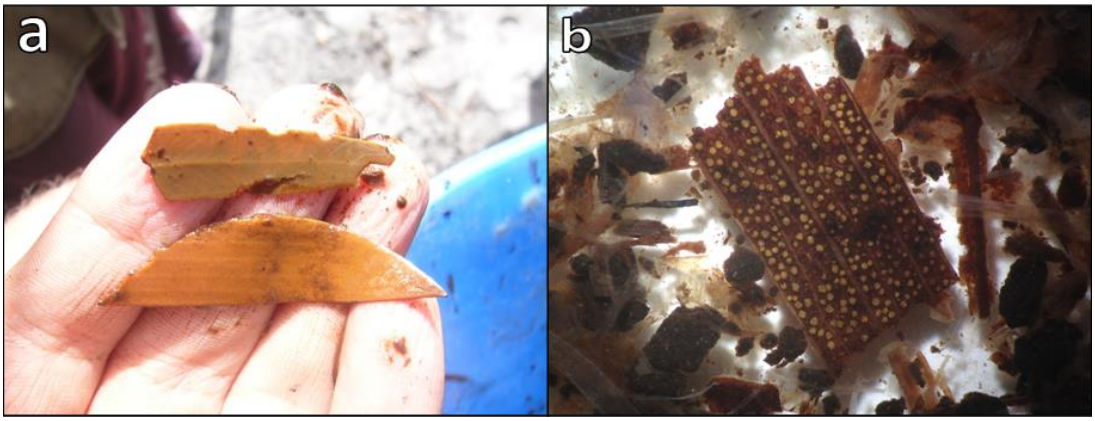

Figure 3: (a) Subfossil eucalyptus leaf (top) in comparison to a subfossil *M. quninquenervia* leaf (bottom). (b) Leaf fragment from SL-15/2 - 78 cm (789 CE) showing main features used to identify species; colouration, five veins and oil glands.

Radiocarbon Dating

Preliminary dating was conducted first on three samples from the core. Approximately 60 mg of dried *M. quinquenervia* leaf material from 23, 58 and 90 cm depths was sent for Accelerator Mass Spectrometry (AMS) radiocarbon dating at Waikato Radiocarbon Dating Laboratory, University of Waikato, New Zealand to establish a preliminary age-depth model. Based on the initial age-depth model, key depths of interest were selected and material from 3, 8, 15, 21, 29, 41, 63, 65, 70 and 84 cm depths was taken to the Australian Institute of Nuclear Science and Engineering, The Australian Nuclear Science and Technology Organisation (ANSTO) to establish a robust age-depth model.

At ANSTO, using an electronic balance, 0.05 g of dried *M. quinquenervia* was weighed out into 50 mL centrifuge tubes. Samples were chemically pre-treated to prepare them for radiocarbon dating. Each sample was treated with 2M HCl at 60°C for 2 hours to remove any carbonate contaminants. Next, they were rinsed three times in purified water and then, to remove any acidic contaminants, given three 60°C, 2 hour treatments in 0.5% NaOH and multiple 60°C, 2 hour treatments in 1% NaOH, until the resulting solutions were clear. The samples were next treated for 2-4 hours with 2M HCl at room temperature to remove any absorbed atmospheric CO_2, rinsed three times in purified water and dried overnight in glass vials capped loosely with Al foil.

Once dried, leaves were loaded into quartz tubes with CuO fuel, and Ag and Cu wires to precipitate any NO_x and SO_x escaping the sample during combustion. The samples were then placed under a vacuum using a vacuum line and the tubes were flame sealed. Then each sample ampule was fired in a furnace overnight at 900°C to oxidise the sample to CO_2.

After the samples had been converted to CO_2, the quartz ampules were loaded into the vacuum line again where the tube was broken and the sample gas sent through a series of two traps. The first trap used dry ice slurry to remove H_2O, and the second trap used liquid nitrogen to remove the CO_2. The rest of the reaction products were allowed to vent and then the CO_2 was quantitatively transferred into a glass tube and reduced to graphite through reaction with H_2 at 600^{o}C using an Fe catalyst. The sample was then

pressed on a cathode and taken for AMS radiocarbon dating on site at ANSTO. Full descriptions of these methods are included in Appendix B.

Age calibration of the 13 ^{14}C AMS samples was performed by Quan Hua using the SH Zone 1-2 bomb ^{14}C data (Hua et al. 2013) extended back in time using SHCal13 (Hogg et al. 2013) and the OxCal program v.4.2 (Bronk Ramsey 2009). Using the OxCal program, an age-depth model was constructed with the OxCal Bayesian P_deposition model with variable rigidity (k parameter) (Bronk Ramsey and Lee 2013). OxCal reported the validity of the model in terms of an agreement index (A_{model}), based on minimizing the overlap between the model probability distribution and the probability distribution of a 'null' model where no constraints or interrelationships were specified. The accepted minimum A_{model} value for an accurate age-depth model is 60 % (Bronk Ramsey 2008).

Isotopic Analysis

Dried leaf material (5 mg) from each sample was ground and homogenised in a 2 mL centrifuge tube with two 3 mm ball bearings on a Retch Ball Milling Machine at 27 Hz for 30 seconds (Appendix B). The homogenised samples were then loaded into tin capsules for Elemental Analysis – Isotope Ratio Mass Spectrometry (EA-IRMS) on a EuroVector EuroEA Elemental Analyser in line with a Nu Instruments, Nu Horizon series continuous-flow mass spectrometer.

Processing of isotopic data included corrections based on measurements of reference gas taken before and after the sample run and measurements of glutamic acid ($C_5H_9NO_4$), Triphenylamine ($C_{18}H_{15}N$) and Glycine ($C_2H_5NO_2$) standards. These

standards were included within the sample runs. The resultant data is reported in $\delta^{13}C$ values, with units of per mil (‰ VPDB). The lab running-average precision of the instruments on which these measurements were determined was ± 0.05 ‰.

Early diagenesis, including the initial changes of organic compounds following the death of the source organism, is known to affect the carbon isotope composition of bulk leaf material (Cranwell 1981; Benner et al. 1990). To determine the amount of early diagenesis undergone by leaves in the study location, a comparison was made between the $\delta^{13}C$ values of leaves collected from trees on the banks of Swallow Lagoon in March 2014 (Andrae 2014) and the $\delta^{13}C$ of leaves taken from the sediment-water interface in the same year (Table 4). The lake bottom leaves appeared visually similar to those collected from the sediment core, both ranging in colour from dark brown to orange and softer than those taken from the trees. The comparison showed 0.95 ‰ depletion in ^{13}C due to early diagenesis. The $\delta^{13}C$ values from leaves from the sediment core were adjusted by the addition of a 1 ‰ offset to enable application of a rainfall-Δ calibration based on unaltered leaves (Tibby et al. in review).

Table 4: The $\delta^{13}C$ (‰) of samples from Swallow Lagoon lake bottom leaves and the leaves taken from trees surrounding the lake, used to calculate the digenesis offset of 1 ‰.

	Tree Leaves	Lake Leaves
$\delta^{13}C$ (‰)	-31.27	-32.02
	-32.02	-31.72
	-29.47	-31.56
		-32.18
Average	-30.92	-31.87
σ	1.31	0.28
Offset	0.95	

Historical Period Rainfall Reconstruction

Bulk leaf $\delta^{13}C$ values obtained from isotopic analysis were used to calculate carbon isotope discrimination ($\Delta_{calculated}$) as outlined in Equation 3. Values for the atmospheric $\delta^{13}C$ used in this equation were obtained from several sources, to match the modelled ages of each sample. For the more recent section of core, post 1994, corresponding data collected at Cape Grim, Tasmania, Australia were available from the GlobalView climate database (GLOBALVIEW-CO2C13 2013), hosted by the National Oceanic & Atmospheric Administration (2015). For older samples, the data collected from Antarctic ice cores were used; DE08, DE08-2 and DSS (Francey et al. 1999) and EPICA Dome C (Elsig et al. 2009).

Atmospheric pCO_2 from historical air sampling and ice core records was used to calculate a predicted discrimination value ($\Delta_{predicted}$) for the year corresponding to each sample using Equation 4. Values for atmospheric pCO_2 post 1976 at Cape Grim were available (Dunse et al. 2005), and downloaded from the Commonwealth Scientific and Industrial Research Organisation (2015). For samples predating these measurements, data from several Antarctic ice cores covered the necessary time interval; Law Dome for samples up to 1000 years old (Etheridge et al. 1996) and EPICA Dome C and DML (Monnin et al. 2004) for older samples.

Using Equation 5, the discrimination anomaly between the Δ values calculated based on $\delta^{13}C$ and the predicted Δ values based on pCO_2 was used to calculate the average precipitation for the 3 year growing period of the leaves. This was used to infer precipitation over the period covered by historic records (1911-2013 CE). This

reconstruction was compared to the instrumental precipitation data taken from the SILO climate database hosted by the Queensland Government Department of Science Information Technology and Innovation (2015). SILO is a patched point dataset and data drill containing Australian climate data from 1889 to present (Jeffrey et al. 2001). The reconstruction was also compared to the records of two nearby Bureau of Meteorology stations. These were Toowong Bowls Club (BOM # 040245) (S 27.49, E 152.99) on the mainland, with a continuous record covering 1889-1999 CE, and from NSI, with a record covering 1947-2015 CE, Point Lookout Bowls Club (BOM # 040175) (S 27.43, E 153.52), taken from Climate Data Online (Bureau of Meteorology 2015b)

To compare these precipitation records to the reconstructed precipitation values, the sedimentation rates drawn from the age-depth model were used to determine how many years were represented by each one centimetre sample. Each time interval was assigned a minimum and maximum age corresponding to the midpoint between the median modelled age of the sample and those of the samples above and below it. As the reconstructed precipitation from each sample is an average of the values predicted over these time intervals, the precipitation records taken from the SILO and BOM databases were also averaged over these intervals. This time-averaging approach enabled direct comparison between the reconstructed precipitation and the actual historic records.

Late-Holocene Rainfall Reconstruction

Bulk leaf $\delta^{13}C$ values from the older core section were combined with the atmospheric $\delta^{13}C$ and pCO_2 data (Etheridge et al. 1996; Francey et al. 1999; Monnin et al. 2004; Elsig et al. 2009) and following the approach outlined above, the anomaly between Δ

values was used construct a precipitation reconstruction covering the full length of the core. The full precipitation reconstruction was split into four time periods corresponding to the MCA (950–1250 CE), the MCA-LIA transition period (1250-1500 CE), the LIA (1500–1850 CE), and the Historic Period (1911–2013 CE).
Analysis of each of the four time periods was used to assess the dominant climate states. Average precipitation for each period was calculated and drier periods were interpreted as El Niño-dominated while wetter periods were interpreted as more La Niña-dominated.

OBSERVATIONS AND RESULTS

Radiocarbon Dating

AMS ^{14}C-ages of *M. quinquenervia* leaves from 23 cm, 58 cm and 90 cm depths provided a framework for the age-depth model (Figure 4). This model was constrained by a further ten dates spaced throughout the sediment core (Table 5). The percent Modern Carbon (pMC) for the shallowest dated sample, at 3 cm, was 108 ± 0.27 % returning a median modelled age of -53 ± 1 BP. The conventional radiocarbon age (CRA) for the deepest dated sample, from 90 cm, was 1590 ± 20 BP.

Table 5: The 13 ^{14}C AMS samples with their corresponding laboratory codes. Conventional Radiocarbon Age (BP) is shown with error equal to one standard deviation. Percent Modern Carbon is also reported, along with isotopic fractionation ^{13}C results, obtained from measurements performed on the graphite sample, or bulk leaf carbon (* indicates).

Sample ID	Laboratory Code	CRA (BP)	pMC (%)	$\delta^{13}C$ (‰)
SL-15/2-3	OZ-T094	Modern	-108.02 ± 0.27	-31.6
SL-15/2-8	OZ-T096	Modern	-111.26 ± 0.34	-31.4
SL-15/2-15	OZ-T098	Modern	-113.29 ± 0.27	-29.8
SL-15/2-21	OZ-T099	165 ± 25	-97.95 ± 0.28	-29.4
SL-15/2-23	Wk-41771	176 ± 20	-97.8 ± 0.2	-29.0*
SL-15/2-29	OZ-T100	Modern	-102.53 ± 0.28	-29.7
SL-15/2-41	OZ-T101	230 ± 25	-97.16 ± 0.29	-30.3
SL-15/2-58	Wk-41770	876 ± 20	-89.7 ± 0.2	-29.8*
SL-15/2-63	OZ-T102	995 ± 25	-88.33 ± 0.24	-29.1
SL-15/2-65	OZ-T103	965 ± 30	-88.67 ± 0.31	-29.0
SL-15/2-70	OZ-T104	1200 ± 30	-86.11 ± 0.30	-28.8
SL-15/2-84	OZ-T105	1370 ± 25	-84.31 ± 0.23	-29.7
SL-15/2-90	Wk-41568	1590 ± 20	-82.0 ± 0.2	-29.9*

Sample OZT100 at 29 cm depth returned a pMC indicative of a post 1950 sample (-102.53 ± 0.28 %). An age-depth model including OZT100 had a low agreement index (A_{model}) of 10 %, compared to the accepted level of 60 % for this value (Bronk Ramsey 2008), indicating that the model was unlikely to be accurate. An additional age-depth model was constructed with an outlier function to attempt to correct for the age reversal of OZT100. Similarly, the model agreement index was 15 %, again too low. The date for OZT100 was therefore discarded as an outlier, and not used for the final age-depth modelling. The final constructed model had a very high A_{model} of 97 %, much higher than the accepted levels of 60 % (Bronk Ramsey 2008). Overall, the model provides a time-scale from 514 CE to 2015 CE.

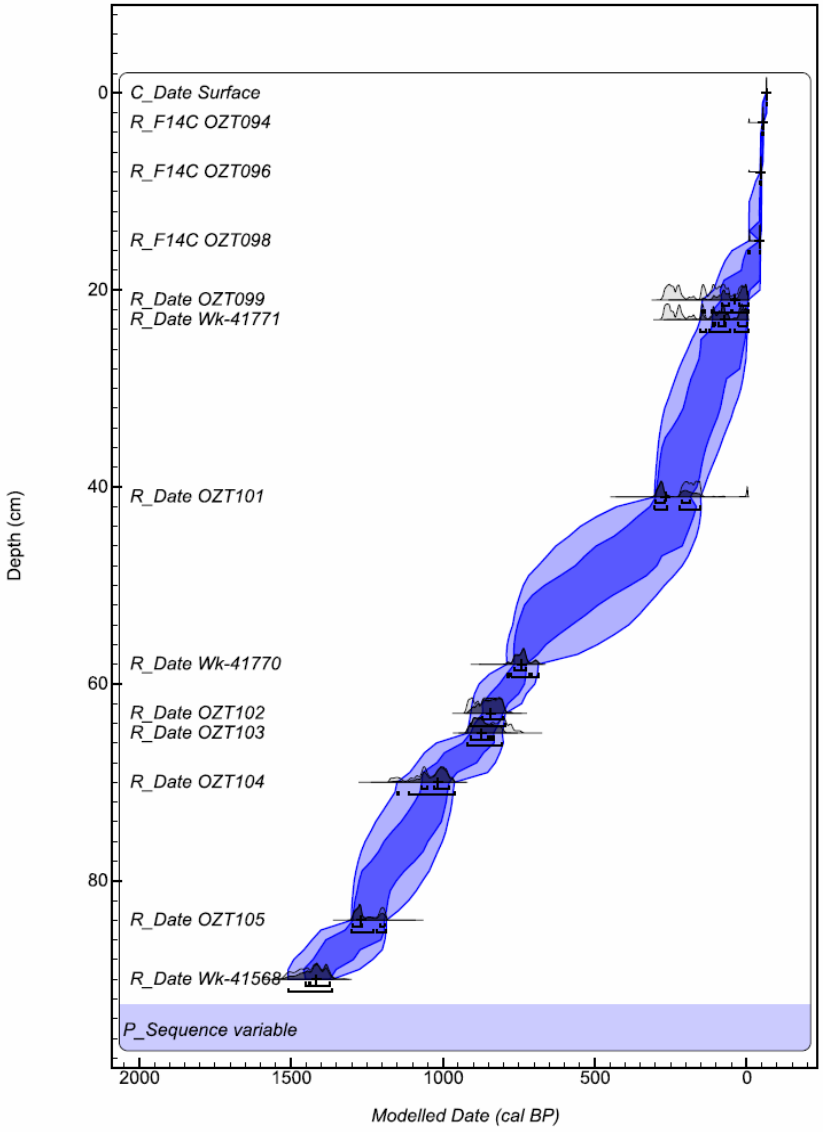

Figure 4: Age-Depth Model for SL-15/2, a 91 cm core from Swallow Lagoon, with dates constrained by twelve ^{14}C AMS radiocarbon dates (3, 8, 15, 21, 23, 41, 58, 63, 65, 70, 84, 90 cm) and the surface (0 cm) set to 2015, the year of collection.

Sedimentation rates are calculated to range from 0.14 to 2.00 cm.year^{-1} (median 1.00 cm.year^{-1}, n = 14) for the top 14 cm of the core, and between 0.02 and 0.17 cm.year^{-1} (median 0.05 cm.year^{-1}, n = 76) lower part of the core. The time interval inferred from these sedimentation rates for each sample ranged from 0-7 years (median 0.75 years, n = 14) for the top 14 cm of the core, and 8-23 years (median 15 years, n = 7) for the remaining historical section, down to 21 cm. For the remaining pre-historical core

sections, samples covered 6-42 years (median 19 years, n = 69). These sedimentation rates are rapid in comparison to rates recorded in other sand island perched lake systems (Donders et al. 2006; Hembrow et al. 2014), especially within the top section of the core. This is consistent with the core being taken from a shallow part of the lake, closer to the shore, where a large amount of sediment may be deposited each year (Björck and Wohlfarth 2001).

Isotopic Analysis

The $\delta^{13}C$ results (Figure 5), corrected for early diagenesis with the addition of 1‰, range between -31.12 and -27.45 ‰ (median -29.26 ‰, σ = 0.81 ‰, n = 91). From these, calculated values for Δ based on Equation 1 range between 21.73 and 24.84 ‰ (median 23.23 ‰, σ = 0.70 ‰, n = 91). The Δ record exhibits both long term trends and abrupt shifts (Figure 6). Complete tables of $\delta^{13}C$ results and values used to determine Δ are included in Appendix C.

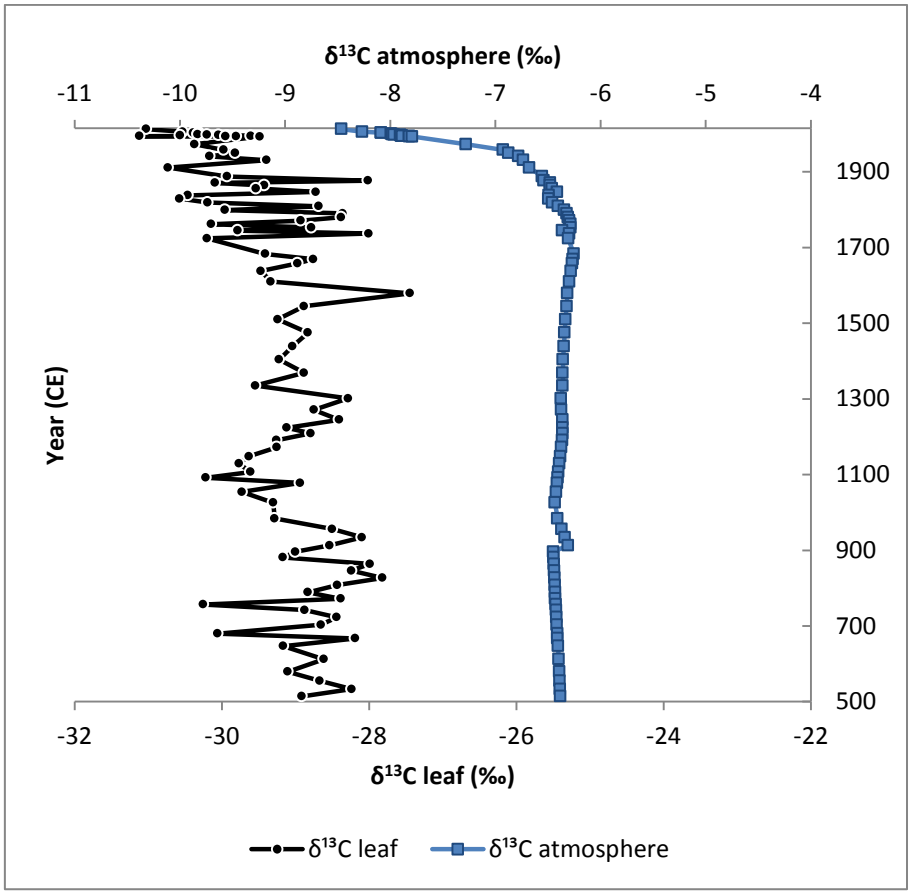

Figure 5: The $\delta^{13}C$ results of bulk leaf tissue for *M. quinquenervia* from SL-15/2 (black), adjusted by the addition of a 1 ‰ offset, shown in relation to the atmospheric $\delta^{13}C$ (blue) used in the calculation of Δ; $\Delta = (\delta^{13}C_{atmosphere} - \delta^{13}C_{plant}) / (1 + \delta^{13}C_{plant} / 1000)$ (Cernusak et al. 2013). Atmospheric $\delta^{13}C$ values are sourced from the GlobalView climate database (GLOBALVIEW-CO2C13 2013), and data collected from Antarctic ice cores DE08, DE08-2 and DSS (Francey et al. 1999) and EPICA Dome C (Elsig et al. 2009).

The record covering the MCA (56-70 cm; 934-1244 CE) has a median Δ of 23.57 ‰ (σ = 0.59 ‰, n = 14). The peak Δ during the MCA occurs at 64 cm (1092 CE) with a value of 24.56 ‰. From the end of the MCA (56 cm; 1244 CE) to the late LIA (29 cm; 1828 CE), the general trend is one of increasing Δ. The peak Δ value of the LIA at 29 cm (1828 CE) is 24.84 ‰. The lowest Δ of the record occurs at 46 cm (1580 CE), within the LIA, with a value of 21.73 ‰. The LIA has a median Δ value of 23.49 ‰ (σ = 0.84 ‰, n = 22). Another low Δ value occurs near the beginning of the historic period, at 23 cm (1876 CE) with a Δ of 22.10 ‰.

The portion of the record covered by the historic meteorological data ranges from 0-21 cm depth (2013-1911 CE) and has a median Δ of 23.03 ‰ (σ = 0.61 ‰, n = 21). The peak Δ value of the historical period occurred at 21 cm (1911 CE) with a value of 24.82 ‰. The lowest value during the historical period is 22.35 ‰, occurring at 15 cm (1993 CE).

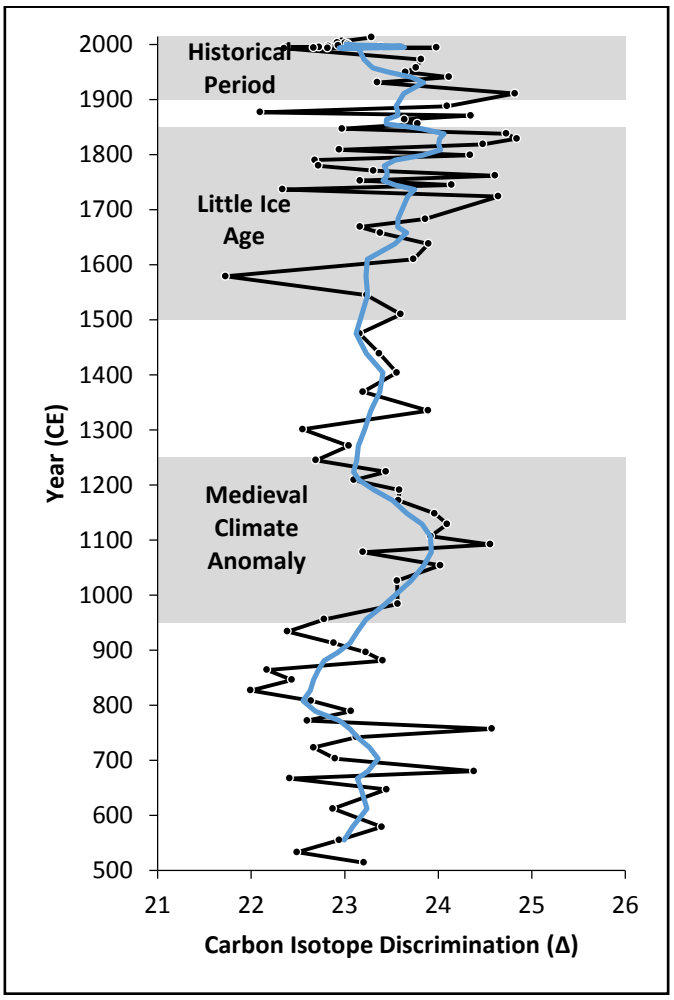

Figure 6: Reconstructed carbon isotope discrimination Δ (‰) in *M. quinquenervia* throughout the length of the 91 cm Swallow Lagoon core, plotted with 2 point centred moving mean (blue). The three focus time-intervals are highlighted in grey. The historical period is defined by the interval 1900-2015 CE, the Little Ice Age covers the 1500-1850 CE interval, and the Medieval Climate Anomaly covers 950-1250 CE.

Historical Period Rainfall Reconstruction

The Δ anomalies for the historical period were compared to time-averaged precipitation records to test the strength of the correlation (Appendix C). The annual precipitation from SILO and BOM datasets were modified by averaging annual records from all years covered the time interval that corresponded to each one centimetre sample, derived from the age-depth model. No significant correlation was found between the Δ anomaly and either SILO or BOM precipitation records (Appendix C; Figure 11).

Although no relationship could be observed on the single sample scale, the rainfall reconstruction derived from the Δ anomaly does appear to reconstruct shifts in rainfall on a decadal to multi-decadal scale (Figure 7). The record was averaged over approximate 20 year bins, except in the most recent decade, and where sample resolution represented a larger time interval.

In the top section of the core, 2003-2014 CE, the average reconstructed rainfall has a mean of 1214 mm (n = 3). This differs from the mean recorded rainfall for the period (1429 mm) by 215 mm, within the 1σ range of the instrumental average (σ = 361 mm). It is worth noting that the three samples from this interval do not fall far from the annual precipitation for the years of their modelled age (2013, 2006, 2004 CE). The high difference between the reconstruction mean and the mean of the record could be explained by the lack of any specific sample from the 2010-2012 CE La Niña. Over the 1984-2003 CE period, the reconstructed mean of 1242 mm (n = 12) differs from the record mean of 1333 mm (σ = 372 mm) by 91 mm, also falling within the 1σ range. Rainfall records show higher mean annual precipitation further back in time, and the

reconstruction appears to agree with greater rainfall before the most recent two decades. The recorded mean rainfall for 1966-1983 CE was 1462 mm, and the reconstruction predicts a mean of 1543 mm (n = 1), over the same interval. This is a difference of 81 mm, within the 1σ range of 406 mm. Similarly, over the period 1946-1965 CE the recorded mean rainfall was 1429 mm (σ = 335 mm), a difference of 138 mm from the mean of the reconstruction, 1567 mm (n = 2).

In all of the past six decades, the reconstructed mean rainfall fell within the range of recorded precipitation. Earlier in the record, the reconstruction fails to predict a short dry period during the interval 1922-1945 CE, which shifts the recorded mean for this interval to 1308 mm. The reconstruction predicts a mean of 1594 mm (n = 2), 286 mm more than recorded, but again within 1σ range (σ = 347 mm). However, the reconstructed mean across 1899-1921 CE of 1855 mm (n = 1) falls 637 mm higher than the recorded average over that period (1218 mm, σ = 308 mm). It seems likely that the divergence from the mean in the lowest interval has been caused by older leaves which have recorded a signal from high rainfall in the decade prior (mean 1712 mm, σ = 509 mm).

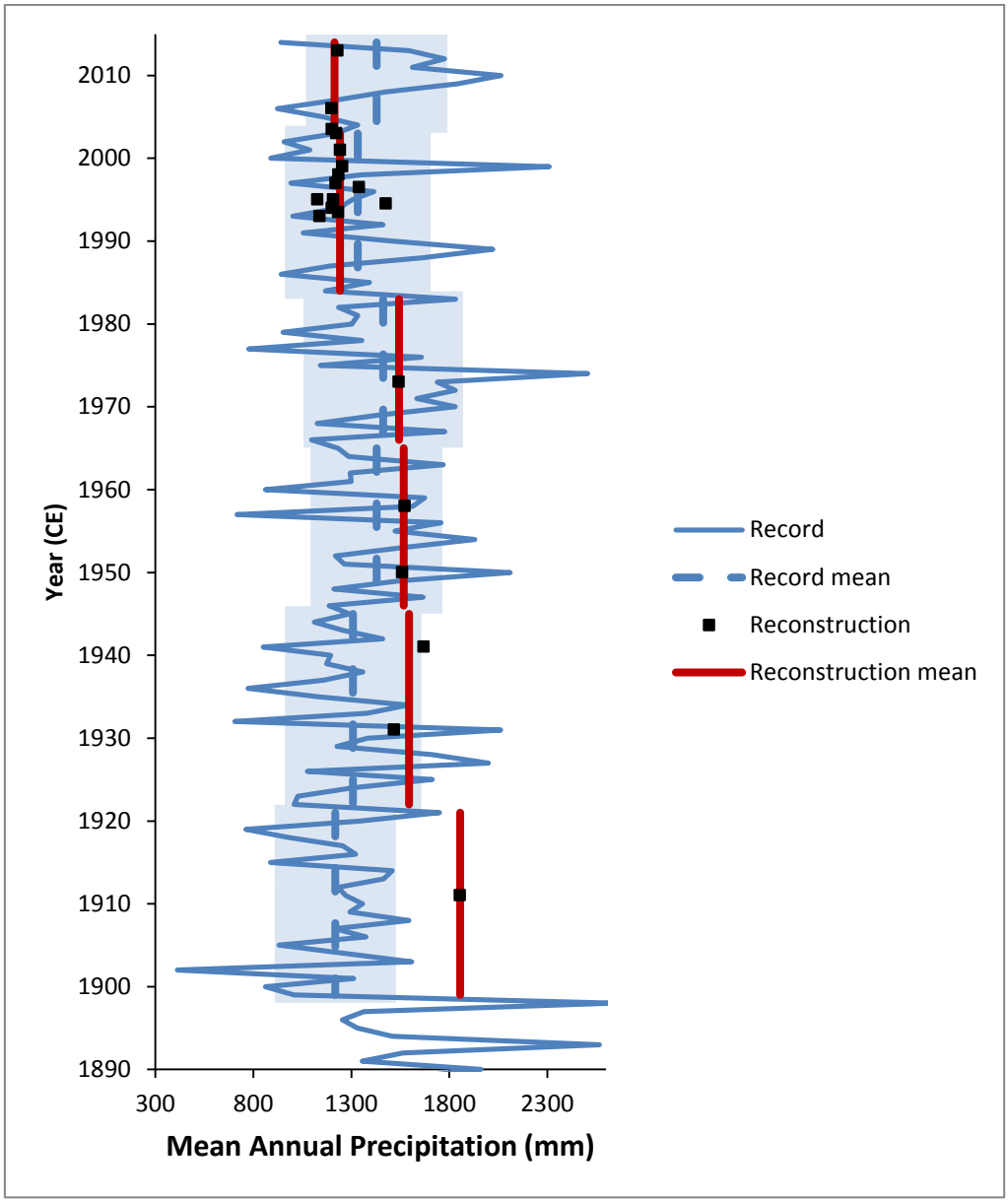

Figure 7: Reconstruction of rainfall over the historical period (black squares) with mean precipitation over ~ 20 year bins (red lines). The annual precipitation record from SILO is shown in blue, with mean precipitation over ~ 20 year bins (dashed blue lines). The mean rainfall predicted over each interval from the reconstruction consistently falls within the 1σ range (light blue boxes) from the historical record, except for the sample centred on 1911 CE, which may be due to older leaves within that layer picking up signals from the high precipitation of the decade prior.

Late-Holocene Rainfall Reconstruction

Although the relationship between Δ anomaly and time-averaged precipitation was not found to be significant on a sample-to-sample scale, the mean reconstructed rainfall over decadal intervals does appear to fall within the range of the historical rainfall

record over the same intervals. As the reconstruction did appear to follow trends on a multi-decadal scale, the model was used to reconstruct rainfall over the Medieval Climate Anomaly, Little Ice Age and historical period (Figure 8).

The rainfall reconstruction for the MCA ranges from 1515 mm in 956 CE to a maximum of 1873 mm in 1092 CE before decreasing to a minimum of 1475 mm in 1245 CE. The median rainfall during the MCA period was 1663 mm (n = 14) and the standard deviation from the MCA mean was 108.6 mm. During the MCA-LIA transition, rainfall increased from a low of 1440 mm at 1301 CE to a high of 1728 mm at 1335 CE but remained relatively drier than the MCA (median 1585 mm, σ = 91 mm, n = 7). The reconstructed rainfall for the LIA drops from 1665 mm in 1510 CE to a minimum of 1273 mm in 1579 CE. The minimum is much lower than the median value of 1654 mm (n = 22) for the LIA. After the early LIA, rainfall increased dramatically to a maximum of 1921 mm in 1829 CE. Standard deviation during the LIA was 180 mm.

The historical period has a minimum rainfall of 1128 mm in 1995 CE and a maximum of 1855 mm in 1911 CE. With a median of 1236 mm (n = 21) of rainfall, the historical period is the driest period in the reconstruction, with all 12 of the driest values occurring within the last two decades of the record (median 1224 mm, σ = 83 mm, n = 15). The median rainfall for the 1911-1973 CE period (n = 6) was 1567 mm, on par with the LIA-MCA transition. The standard deviation over this period was 126 mm.

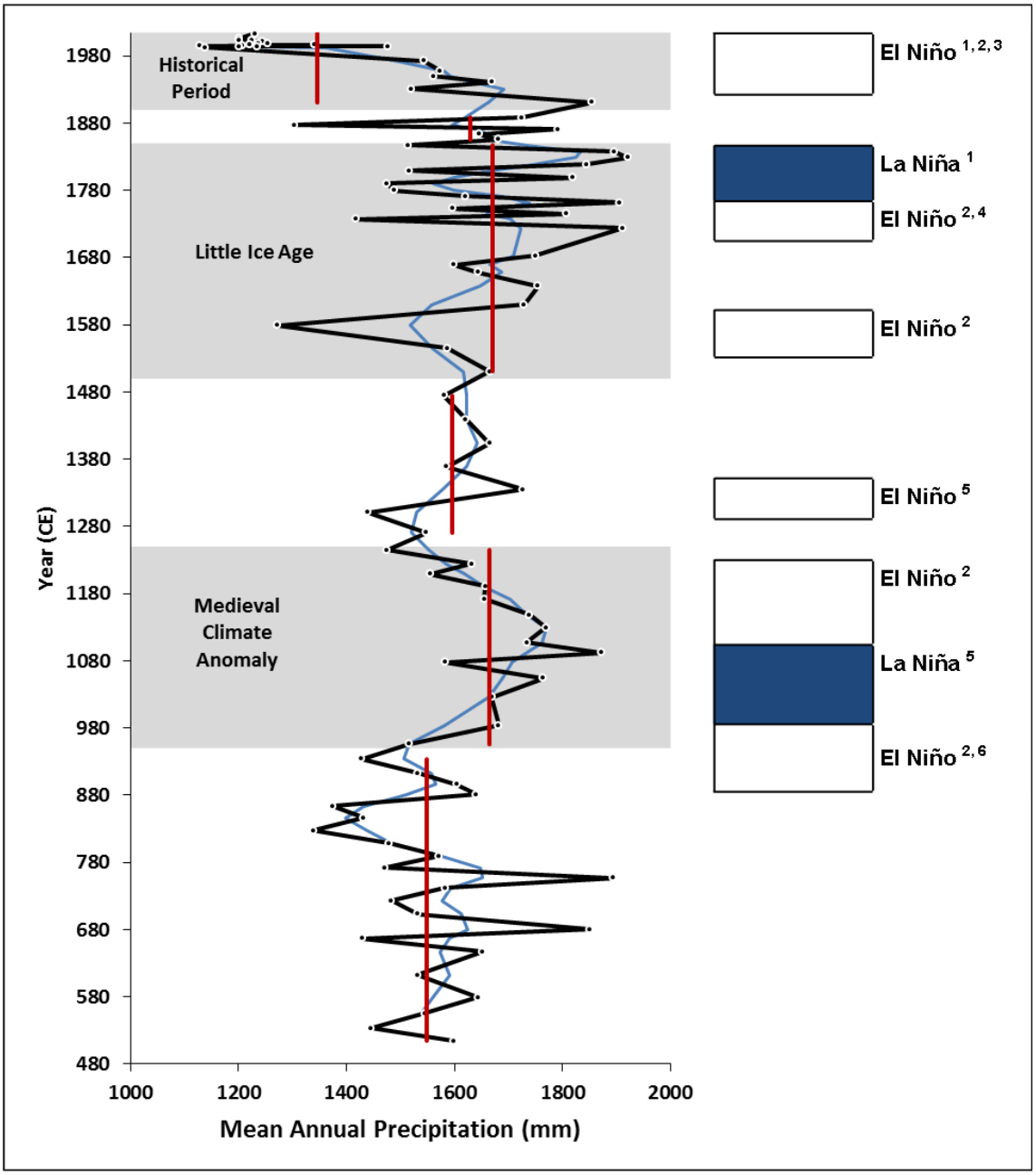

Figure 8: Rainfall reconstruction for full length of the 91 cm core SL-15/2 plotted with a 2 point centred moving mean (blue) and the mean precipitation for each time-period (red). Text to the right of figure indicates wet or dry states predicted in previous studies; [1] Cobb et al. 2003, [2] Vance et al. 2015, [3] Hendy et al. 2002, [4] Osborne et al. 2014, [5] Goodwin et al. 2014, [6] Striewski et al. 2013.

DISCUSSION

To resolve uncertainties about the behaviour of the ENSO system over the past millennium, the $\delta^{13}C$ record from Swallow Lagoon was used to construct a reconstruction of precipitation using the relationship established in modern leaves by Tibby et al. (in review). When compared directly to climate records from Queensland for individual sample durations, the reconstruction performs poorly. One possible explanation is a temporal mismatch between the time of leaf formation and their incorporation into the sediment record. It is suspected that as the core was taken close to the lake shore, leaves which had fallen on the canopy floor may have remained there for some time before being transported into the lake (Orndorff and Lang 1981). It is also possible that the leaves resting on the steep lake bed may slump down from time to time (Björck and Wohlfarth 2001). These effects would introduce older climate signals, and radiocarbon ages, into the record, and distort its resolution.

On a decadal to multi-decadal scale, the reconstruction performs better. Compared to the climate records from the region, the reconstruction does reflect changes in the mean climate state from wetter in the mid twentieth century to drier over the past two decades. Mean average rainfall for the reconstruction fits within the standard deviation from the mean of the instrumental data, except for the interval 1899-1921 CE, which could be due to the temporal mismatching described above. Unfortunately the multi-decade resolution this produces is not enough to pick up high frequency changes in the variability of the ENSO cycle, but it does give an indication of average climate states on a scale small enough to study the MCA and LIA.

Extending the reconstruction back, the rainfall reconstruction agrees with studies which find a predominantly dry climate at the onset of the MCA (Cobb et al. 2003; Allen 2006). Average ENSO conditions appear to shift to more La Niña-dominant phases, becoming wetter until approximately 1100 CE, corresponding to similar findings in recent multi-proxy data collected from locations across the Southern Hemisphere (Goodwin et al. 2014). The resolution of the reconstruction over the MCA is not high enough to distinguish many of the individual El Niño events shown in recent studies (Mann et al. 2005; Mann et al. 2012; Striewski et al. 2013), although there is a mid-900s dry period corresponding to low precipitation in the maar lake laminae record of Striewski et al. (2013). A mega-drought between 1174-1212 (Vance et al. 2015), is also observed as declining precipitation levels toward the end of the MCA.

The rainfall reconstruction is in agreement with the multi-proxy record of Goodwin et al. (2014), who showed a dry El Niño event during the LIA-MCA transition ca. 1300 CE, and with fossil coral $\delta^{18}O$ signatures that suggest the climate became wetter over the course of the LIA (Cobb et al. 2003). The coral $\delta^{18}O$ record of Osborne et al. (2014) showed that the driest period during the late LIA (1793-1850) was the decade 1810-1820. The reconstruction presented here is consistent with low rainfall around this time, although the driest period of the LIA was found to have occurred prior to the commencement of the coral record, during the late 1500s. This dry period occurs too late to match an early 1500s mega-drought shown by Vance et al. (2015), but the reconstruction does show below average rainfall over the timeframe given in their record. A mega drought in the early 1700s reported by Vance et al. (2015) does correspond to a dry period in this reconstruction.

The hypothesis that high precipitation would be observed during the MCA was supported. These findings would indicate La Niña dominance during the MCA, and are supported by the majority of prior research (Cobb et al. 2003; Mann et al. 2005; Carrillo-Bastos et al. 2013; Thompson et al. 2013). The hypothesis of a dry LIA was not supported, with many of the wettest years of the reconstruction occurring within the late LIA. This is indicative of a La Niña-dominated climate state during the LIA. These findings support the minority of paleoclimate reconstructions (Neukom et al. 2011; Emile-Geay et al. 2013; Lorrey et al. 2013; Vance et al. 2013) Overall, the mean climate states in Australia during the LIA and MCA were found to be very similar in this reconstruction. These findings support an internally variable ENSO system, apparently not responding to the external (solar or volcanic) forcing over the last millennium which drove global temperatures during the MCA and LIA (Clement et al. 1996; Cobb et al. 2003; Mann et al. 2005). It appears as though the east–west SST gradient across the Pacific is not causing ENSO responses in a manner predicted by the ocean dynamical thermostat hypothesis.

The hypothesis that the historical period was drier on average than the rest of the millennium was supported by the reconstruction. With a lower average precipitation over the 1900s and the lowest levels of precipitation occurring within the past two decades, this would indicate an increase in El Niño dominance. These findings are in agreement with the majority of paleoclimate records and highlight the historical period as an unusual case (Linsley et al. 2000; Hendy et al. 2002; Cobb et al. 2003; Mann et al. 2005; Neukom et al. 2011; Emile-Geay et al. 2013; Lorrey et al. 2013; Vance et al.

2013; Dassié et al. 2014). Although external forcing appeared to have no impact on MCA or LIA ENSO patterns, this does not seem to be the case for the historical period.

The findings presented here follow the assumption that the reconstruction based on the Equation 5 is accurate. This is assumed to be true for multi-decade scale shifts in climate state, although the resolution given by single samples could not be shown to be significant. There were not enough multi-decadal cycles covered by the historical record to test the significance of the assumed relationship directly. As a test of whether bulk leaf $\delta^{13}C$ observed in sub-fossil *M. quinquenervia* leaves relates to precipitation in the same way as modern leaves do, the modern analysis certainly raises questions about the applicability of the Tibby et al. (in review) calibration for predicting rainfall at a high resolution in settings where older leaves may frequently be re-deposited. The approach may still be useful for resolving longer timescale changes to the ENSO system, as the mean of the reconstruction does fall within the range of the historical dataset.

A higher resolution reconstruction may be produced by looking at the results from SL-15/1, taken from deeper in the lake, where the influx of old leaves from the shore would not distort the record so much. However, as the reconstruction is based on a calibration from modern leaves, a better understanding of the effect early diagenesis has on ^{13}C with increasing depth. If this could be defined beyond the 1 ‰ offset seen in leaves from the sediment-water interface, it may be possible to apply corrections to the isotopic values recovered, and the reconstruction calibrated on modern leaves may be more applicable than was found in this thesis.

CONCLUSIONS

In this thesis, bulk leaf $\delta^{13}C$ data from *M. quinquenervia* leaves collected in subtropical Australia were used to investigate precipitation changes in the region as an indication of shifts in ENSO state over the past millennium. Changes in precipitation were reconstructed using a previously established relationship between bulk leaf Δ and rainfall in modern *M. quinquenervia* leaves. The relationship was not significant on a sub-decadal scale when the reconstruction was used on sub-fossil *M. quinquenervia* preserved from the historic period. In contrast, on a multi-decadal scale, the reconstruction seems to follow shifts from periods of high to low rainfall in the historic data and in existing proxy records from the late Holocene. The rainfall reconstruction created for this thesis indicated that eastern Australia received higher precipitation during the Medieval Climate Anomaly and the Little Ice Age, relative to the past century. These results also show that the past two decades have had the lowest average rainfall in the past millennium. This indicates a shift from a La Niña dominant climate state over the late-Holocene, to a modern El Niño dominated state.

This thesis has provided a high resolution, quantitative precipitation reconstruction for south-east Queensland. This record is almost unique among Australian lake records in that it includes internal validation against the historical record within the top 20 cm of the core (Tibby pers. comm., 22 September 2015). This provides an important terrestrial palaeoclimate proxy which sheds light on shifts in mean ENSO states during the past millennium. External forcing during the MCA and LIA did not appear to change ENSO patterns in a manner consistent with the ocean dynamic thermostat hypothesis. Rather, little difference was observable in the average climate experienced in eastern Australia

over these periods. The reconstruction does show a marked shift towards drier conditions corresponding to the onset of anthropogenic climate change suggesting an increase in El Niño dominance. This raises questions about just how different modern conditions are that those in the past. Eastern Australia's climate is highly sensitive to ENSO dynamics and so future intensification of the ENSO system will have a strong effect on precipitation across eastern Australia.

ACKNOWLEDGMENTS

The author is grateful to the Minjerribah Moorgumpin elders for permission to work on North Stradbroke Island. Special thanks to John Tibby, Cameron Barr and Richard Lewis (University of Adelaide) and John Marshall and Glenn McGregor (Queensland Department of Science, Information Technology and Innovation) for field assistance in coring Swallow Lagoon. I also extend thanks to Patrick Moss, Changi Weereseena, Rebecca Farrell, Emily Field, Jie Chang (University of Queensland), Lynda Petherick (Xi'an Jiaotong - Liverpool University), Matt Jones (University of Nottingham) and Paul Smith and Daniel Carter (Sibelco Australia) for their field assistance. The project was conducted under the supervision of Francesca McInerney and John Tibby, who provided excellent guidance and advice throughout. The author is thankful for the laboratory assistance of Kristine Nielson, Jake Andrae and Stefan Caddy-Retalic. Isotope analysis was performed by Mark Rollog (University of Adelaide). Preliminary radiocarbon dating was conducted by Alan Hogg at Waikato Radiocarbon Dating Laboratory, University of Waikato, New Zealand. Further radiocarbon dating was performed during a visit to AINSE with guidance from Quan Hua, and laboratory assistance from Shwaron Kumar and Prabha Pratap. The author would like to thank AINSE Ltd for financial assistance (Award No ALNGRA15524) to enable this radiocarbon dating.

REFERENCES

ALLEN M. S. 2006. New ideas about late Holocene climate variability in the central Pacific. *Current Anthropology* **47**, 521-535.
ANDRAE J. W. 2014. Chemical signatures of Melaleuca quinquenervia leaves as precipitation proxies. Honours thesis, University of Adelaide, Adelaide (unpubl.).
ARENS N. C., HOPE JAHREN A. & AMUNDSON R. 2000. Can C3 plants faithfully record the carbon isotopic composition of atmospheric carbon dioxide? *Paleobiology* **26**, 137-164.
BARBOUR M. M. 2007. Stable oxygen isotope composition of plant tissue: a review. *Functional Plant Biology* **34**, 83-94.
BARR C. 2012. An island of opportunity: A concentration of late Quaternary sediment sites on North Stradbroke Island, Australia. *Quaternary International* **279**, p.40.
BENNER R., WELIKY K. & HEDGES J. I. 1990. Early diagenesis of mangrove leaves in a tropical estuary: molecular-level analyses of neutral sugars and lignin-derived phenols. *Geochimica et Cosmochimica Acta* **54**, 1991-2001.

BIRKS H. 1998. DG Frey and ES Deevey Review 1: Numerical tools in palaeolimnology–Progress, potentialities, and problems. *Journal of Paleolimnology* **20**, 307-332.
BJÖRCK S. & WOHLFARTH B. 2001. 14C chronostratigraphic techniques in paleolimnology. *Tracking environmental change using lake sediments.* pp. 205-245. Springer, Netherlands.
BRONK RAMSEY C. 2008. Deposition models for chronological records. *Quaternary Science Reviews* **27**, 42-60.
BRONK RAMSEY C. 2009. Bayesian analysis of radiocarbon dates. *Radiocarbon* **51**, 337-360.
BRONK RAMSEY C. & LEE S. 2013. Recent and planned developments of the program OxCal. *Radiocarbon* **55**, 720-730.
BUREAU OF METEOROLGY 2015. La Niña – Detailed Australian Analysis. <http://www.bom.gov.au/climate/enso/lnlist/>. (retrieved 10 October 2015).
BUREAU OF METEOROLOGY 2015. Climate Data Online. <http://www.bom.gov.au/climate/data>. (retrieved 10 June 2015).
CANE M. A. 2005. The evolution of El Niño, past and future. *Earth and Planetary Science Letters* **230**, 227-240.
CARRILLO-BASTOS A., ISLEBE G. A. & TORRESCANO-VALLE N. 2013. 3800 Years of Quantitative Precipitation Reconstruction from the Northwest Yucatan Peninsula. *PloS one* **8**.
CERNUSAK L. A., WINTER K., ARANDA J. & TURNER B. L. 2008. Conifers, angiosperm trees, and lianas: growth, whole-plant water and nitrogen use efficiency, and stable isotope composition (δ13C and δ18O) of seedlings grown in a tropical environment. *Plant Physiology* **148**, 642-659.
CERNUSAK L. A., UBIERNA N., WINTER K., HOLTUM J. A., MARSHALL J. D. & FARQUHAR G. D. 2013. Environmental and physiological determinants of carbon isotope discrimination in terrestrial plants. *New Phytologist* **200**, 950-965.
CHEN D., CANE M. A., KAPLAN A., ZEBIAK S. E. & HUANG D. 2004. Predictability of El Niño over the past 148 years. *Nature* **428**, 733-736.
CHIANG J. C. 2009. The tropics in paleoclimate. *Annual Review of Earth and Planetary Sciences* **37**, 263-297.
CHIEW F. H., PIECHOTA T. C., DRACUP J. A. & MCMAHON T. A. 1998. El Nino/Southern Oscillation and Australian rainfall, streamflow and drought: Links and potential for forecasting. *Journal of Hydrology* **204**, 138-149.
CLEMENT A. C., SEAGER R., CANE M. A. & ZEBIAK S. E. 1996. An ocean dynamical thermostat. *Journal of Climate* **9**, 2190-2196.
COBB K. M., CHARLES C. D., CHENG H. & EDWARDS R. L. 2003. El Nino/Southern Oscillation and tropical Pacific climate during the last millennium. *Nature* **424**, 271-276.
COBB K. M., WESTPHAL N., SAYANI H. R., WATSON J. T., DI LORENZO E., CHENG H., EDWARDS R. & CHARLES C. D. 2013. Highly variable El Niño–Southern Oscillation throughout the Holocene. *Science* **339**, 67-70.
COMMONWEALTH SCIENTIFIC AND INDUSTRIAL RESEARCH ORGANISATION 2015. Cape Grim Greenhouse Gas Data. <http://www.csiro.au/greenhouse-gases/>. (retrieved 17 May 2015).
COX M. E., JAMES A., HAWKE A., SPECHT A., RAIBER M. & TAULIS M. 2011. North Stradbroke Island 3D hydrology: surface water features, settings and groundwater links. *Proceedings of the Royal Society of Queensland* **117**, 47-64.
CRANWELL P. 1981. Diagenesis of free and bound lipids in terrestrial detritus deposited in a lacustrine sediment. *Organic Geochemistry* **3**, 79-89.
DASSIÉ E. P., LINSLEY B. K., CORRÈGE T., WU H. C., LEMLEY G. M., HOWE S. & CABIOCH G. 2014. A Fiji multi‐coral δ18O composite approach to obtaining a more accurate reconstruction of the last two‐centuries of the ocean‐climate variability in the South Pacific Convergence Zone region. *Paleoceanography* **29**, 1196-1213.
DIAZ H. F., HOERLING M. P. & EISCHEID J. K. 2001. ENSO variability, teleconnections and climate change. *International Journal of Climatology* **21**, 1845-1862.
DIEFENDORF A. F., MUELLER K. E., WING S. L., KOCH P. L. & FREEMAN K. H. 2010. Global patterns in leaf 13C discrimination and implications for studies of past and future climate. *Proceedings of the National Academy of Sciences* **107**, 5738-5743.
DONDERS T. H., WAGNER F. & VISSCHER H. 2006. Late Pleistocene and Holocene subtropical vegetation dynamics recorded in perched lake deposits on Fraser Island, Queensland, Australia. *Palaeogeography, Palaeoclimatology, Palaeoecology* **241**, 417-439.

DONDERS T. H., HABERLE S. G., HOPE G., WAGNER F. & VISSCHER H. 2007. Pollen evidence for the transition of the Eastern Australian climate system from the post-glacial to the present-day ENSO mode. *Quaternary Science Reviews* **26**, 1621-1637.
DUNSE B., STEELE L., WILSON S., FRASER P. & KRUMMEL P. 2005. Trace gas emissions from Melbourne, Australia, based on AGAGE observations at Cape Grim, Tasmania, 1995–2000. *Atmospheric environment* **39**, 6334-6344.
ELSIG J., SCHMITT J., LEUENBERGER D., SCHNEIDER R., EYER M., LEUENBERGER M., JOOS F., FISCHER H. & STOCKER T. F. 2009. Stable isotope constraints on Holocene carbon cycle changes from an Antarctic ice core. *Nature* **461**, 507-510.
EMILE-GEAY J., COBB K. M., MANN M. E. & WITTENBERG A. T. 2013. Estimating Central Equatorial Pacific SST Variability over the Past Millennium. Part II: Reconstructions and Implications. *Journal of Climate* **26**, 2329-2352.
ETHERIDGE D., STEELE L., LANGENFELDS R., FRANCEY R., BARNOLA J. M. & MORGAN V. 1996. Natural and anthropogenic changes in atmospheric CO2 over the last 1000 years from air in Antarctic ice and firn. *Journal of Geophysical Research: Atmospheres (1984–2012)* **101**, 4115-4128.
FARQUHAR G. D., O'LEARY M. & BERRY J. 1982. On the relationship between carbon isotope discrimination and the intercellular carbon dioxide concentration in leaves. *Functional Plant Biology* **9**, 121-137.
FARQUHAR G. D., EHLERINGER J. R. & HUBICK K. T. 1989. Carbon isotope discrimination and photosynthesis. *Annual review of plant biology* **40**, 503-537.
FRANCEY R., ALLISON C., ETHERIDGE D., TRUDINGER C., ENTING I., LEUENBERGER M., LANGENFELDS R., MICHEL E. & STEELE L. 1999. A 1000‐year high precision record of δ13C in atmospheric CO2. *Tellus B* **51**, 170-193.
GALLANT A. J., PHIPPS S. J., KAROLY D. J., MULLAN A. B. & LORREY A. M. 2013. Nonstationary Australasian teleconnections and implications for paleoclimate reconstructions. *Journal of Climate* **26**, 8827-8849.
GLOBALVIEW-CO2C13 2013. Cooperative Global Atmospheric Data Integration Project. Boulder, Colorado, U.S.A.
GOODWIN I. D., BROWNING S., LORREY A. M., MAYEWSKI P. A., PHIPPS S. J., BERTLER N. A., EDWARDS R. P., COHEN T. J., VAN OMMEN T. & CURRAN M. 2014. A reconstruction of extratropical Indo-Pacific sea-level pressure patterns during the Medieval Climate Anomaly. *Climate Dynamics* **43**, 1197-1219.
HEMBROW S. C., TAFFS K. H., ATAHAN P., PARR J., ZAWADZKI A. & HEIJNIS H. 2014. Diatom community response to climate variability over the past 37,000 years in the sub-tropics of the Southern Hemisphere. *Science of the Total Environment* **468**, 774-784.
HENDY E. J., GAGAN M. K., ALIBERT C. A., MCCULLOCH M. T., LOUGH J. M. & ISDALE P. J. 2002. Abrupt decrease in tropical Pacific sea surface salinity at end of Little Ice Age. *Science* **295**, 1511-1514.
HOGG A. G., HUA Q., BLACKWELL P. G., NIU M., BUCK C. E., GUILDERSON T. P., HEATON T. J., PALMER J. G., REIMER P. J. & REIMER R. W. 2013. SHCal13 Southern Hemisphere calibration, 0–50,000 years cal BP. *Radiocarbon*.
HUA Q., BARBETTI M. & RAKOWSKI A. Z. 2013. Atmospheric radiocarbon for the period 1950–2010. *Radiocarbon* **55**, 2059-2072.
JEFFREY S. J., CARTER J. O., MOODIE K. B. & BESWICK A. R. 2001. Using spatial interpolation to construct a comprehensive archive of Australian climate data. *Environmental Modelling & Software* **16**, 309-330.
KHIDER D., STOTT L., EMILE‐GEAY J., THUNELL R. & HAMMOND D. 2011. Assessing El Niño Southern Oscillation variability during the past millennium. *Paleoceanography* **26**.
KOUTAVAS A. & JOANIDES S. 2012. El Niño–Southern Oscillation extrema in the Holocene and Last Glacial Maximum. *Paleoceanography* **27**.
LEACH L. 2011. Hydrology and physical setting of North Stradbroke Island. *Proceedings of the Royal Society of Queensland* **117**, 21-46.
LINSLEY B. K., WELLINGTON G. M. & SCHRAG D. P. 2000. Decadal sea surface temperature variability in the subtropical South Pacific from 1726 to 1997 AD. *Science* **290**, 1145-1148.
LIU Z. 2012. Dynamics of interdecadal climate variability: A historical perspective*. *Journal of Climate* **25**, 1963-1995.
LIU Z., LU Z., WEN X., OTTO-BLIESNER B., TIMMERMANN A. & COBB K. 2014. Evolution and forcing mechanisms of El Nino over the past 21,000 years. *Nature* **515**, 550-553.

LORREY A., FAUCHEREAU N., STANTON C., CHAPPELL P., PHIPPS S., MACKINTOSH A., RENWICK J., GOODWIN I. & FOWLER A. 2013. The Little Ice Age climate of New Zealand reconstructed from Southern Alps cirque glaciers: a synoptic type approach. *Climate Dynamics* **42**, 3039-3060.
LOUGH J. M. 2011. Great Barrier Reef coral luminescence reveals rainfall variability over northeastern Australia since the 17th century. *Paleoceanography* **26**, n/a-n/a.
MANN M. E., CANE M. A., ZEBIAK S. E. & CLEMENT A. 2005. Volcanic and solar forcing of the tropical Pacific over the past 1000 years. *Journal of Climate* **18**, 447-456.
MANN M. E., FUENTES J. D. & RUTHERFORD S. 2012. Underestimation of volcanic cooling in tree-ring-based reconstructions of hemispheric temperatures. *Nature Geoscience* **5**, 202-205.
MARSHALL J. C. & MCGREGOR G. B. 2011. The influence of water depth on the distribution of the emergent sedge'Lepironia articulata'(Cyperaceae) in two dune lakes of southern Queensland Coastal Wallum Wetlands. *Proceedings of the Royal Society of Queensland* **117**, 193-199.
MARSHALL J. D., BROOKS J. R. & LAJTHA K. 2007. Sources of variation in the stable isotopic composition of plants. *Stable isotopes in ecology and environmental science*, 22-60.
MARSHALL J. D., BROOKS J. R. & LAJTHA K. 2008. Sources of variation in the stable isotopic composition of plants. *In* MICHENER R. & LAJTHA K. eds. *Stable isotopes in ecology and environmental science.* pp. 22-60. John Wiley & Sons.
MASON S. J. & GODDARD L. 2001. Probabilistic precipitation anomalies associated with ENSO. *Bulletin of the American Meteorological Society* **82**, 619-638.
MONNIN E., STEIG E. J., SIEGENTHALER U., KAWAMURA K., SCHWANDER J., STAUFFER B., STOCKER T. F., MORSE D. L., BARNOLA J.-M. & BELLIER B. 2004. Evidence for substantial accumulation rate variability in Antarctica during the Holocene, through synchronization of CO 2 in the Taylor Dome, Dome C and DML ice cores. *Earth and Planetary Science Letters* **224**, 45-54.
MOSISCH T. D. & ARTHINGTON A. H. 2001. Polycyclic aromatic hydrocarbon residues in the sediments of a dune lake as a result of power boating. *Lakes & Reservoirs: Research & Management* **6**, 21-32.
MOSS P. T., TIBBY J., PETHERICK L., MCGOWAN H. & BARR C. 2013. Late Quaternary vegetation history of North Stradbroke Island, Queensland, eastern Australia. *Quaternary Science Reviews* **74**, 257-272.
NATIONAL OCEANIC & ATMOSPHERIC ADMINISTRATION 2015. GLOBALVIEW-CO2C13. <http://www.esrl.noaa.gov/gmd/ccgg/globalview/co2c13/co2c13_intro.html>. (retrieved 27 July 2015).
NEUKOM R., LUTERBACHER J., VILLALBA R., KÜTTEL M., FRANK D., JONES P., GROSJEAN M., WANNER H., ARAVENA J.-C. & BLACK D. 2011. Multiproxy summer and winter surface air temperature field reconstructions for southern South America covering the past centuries. *Climate Dynamics* **37**, 35-51.
OCEAN STUDIES BOARD AND MAPPING SCIENCE COMMITTEE 2004. A Geospatial Framework for the Coastal Zone:: National Needs for Coastal Mapping and Charting. National Academies Press.
ORNDORFF K. A. & LANG G. E. 1981. Leaf litter redistribution in a West Virginia hardwood forest. *The Journal of Ecology*, 225-235.
OSBORNE M. C., DUNBAR R. B., MUCCIARONE D. A., DRUFFEL E. & SANCHEZ-CABEZA J.-A. 2014. A 215-yr coral δ18O time series from Palau records dynamics of the West Pacific Warm Pool following the end of the Little Ice Age. *Coral Reefs* **33**, 719-731.
PETHERICK L., MCGOWAN H. & MOSS P. 2008. Climate variability during the Last Glacial Maximum in eastern Australia: evidence of two stadials? *Journal of Quaternary Science* **23**, 787-802.
PETHERICK L. M., MCGOWAN H. A. & KAMBER B. S. 2009. Reconstructing transport pathways for late Quaternary dust from eastern Australia using the composition of trace elements of long traveled dusts. *Geomorphology* **105**, 67-79.
PRENTICE I. C., MENG T., WANG H., HARRISON S. P., NI J. & WANG G. 2011. Evidence of a universal scaling relationship for leaf CO2 drawdown along an aridity gradient. *New Phytologist* **190**, 169-180.
QUEENSLAND GOVERNMENT DEPARTMENT OF SCIENCE INFORMATION TECHNOLOGY AND INNOVATION 2015. SILO climate data. <https://www.longpaddock.qld.gov.au/silo/index.html>. (retrieved 17 May 2015).
RODBELL D. T., SELTZER G. O., ANDERSON D. M., ABBOTT M. B., ENFIELD D. B. & NEWMAN J. H. 1999. An~ 15,000-year record of El Niño-driven alluviation in southwestern Ecuador. *Science* **283**, 516-520.
ROPELEWSKI C. F. & HALPERT M. S. 1989. Precipitation patterns associated with the high index phase of the Southern Oscillation. *Journal of climate* **2**, 268-284.
SCHUBERT B. A. & JAHREN A. H. 2012. The effect of atmospheric CO2 concentration on carbon isotope fractionation in C3 land plants. *Geochimica et Cosmochimica Acta* **96**, 29-43.
STEWART G. R., TURNBULL M., SCHMIDT S. & ERSKINE P. 1995. 13C natural abundance in plant communities along a rainfall gradient: a biological integrator of water availability. *Functional Plant Biology* **22**, 51-55.

STRIEWSKI B., SHULMEISTER J., AUGUSTINUS P. & SODERHOLM J. 2013. Late Holocene climate variability from Lake Pupuke maar, Auckland, New Zealand. *Quaternary Science Reviews* **77**, 46-54.
THOMPSON L. G., MOSLEY-THOMPSON E., DAVIS M. E., ZAGORODNOV V. S., HOWAT I. M., MIKHALENKO V. N. & LIN P. N. 2013. Annually resolved ice core records of tropical climate variability over the past ~1800 years. *Science* **340**, 945-50.
TIBBY J., BARR C., GREENWAY M., HENDERSON A. C. G., LENG M. J., MCINERNEY F. A., MARSHALL J. C., MCGREGOR G. B. & TYLER J. J. in review. A model for quantifying past tropical and sub-tropical rainfall using leaf carbon isotopes from the common paperbark tree, Melaleuca quinquenervia
TUDHOPE A., SHIMMIELD G., CHILCOTT C., JEBB M., FALLICK A. & DALGLEISH A. 1995. Recent changes in climate in the far western equatorial Pacific and their relationship to the Southern Oscillation; oxygen isotope records from massive corals, Papua New Guinea. *Earth and Planetary Science Letters* **136**, 575-590.
TUDHOPE A. W., CHILCOTT C. P., MCCULLOCH M. T., COOK E. R., CHAPPELL J., ELLAM R. M., LEA D. W., LOUGH J. M. & SHIMMIELD G. B. 2001. Variability in the El Niño-Southern Oscillation through a glacial-interglacial cycle. *Science* **291**, 1511-1517.
VANCE T. R., VAN OMMEN T. D., CURRAN M. A. J., PLUMMER C. T. & MOY A. D. 2013. A Millennial Proxy Record of ENSO and Eastern Australian Rainfall from the Law Dome Ice Core, East Antarctica. *Journal of Climate* **26**, 710-725.
VANCE T. R., ROBERTS J. L., PLUMMER C. T., KIEM A. S. & VAN OMMEN T. D. 2015. Interdecadal Pacific variability and eastern Australian megadroughts over the last millennium. *Geophysical Research Letters* **42**, 129-137.
WANNER H., BEER J., BUETIKOFER J., CROWLEY T. J., CUBASCH U., FLUECKIGER J., GOOSSE H., GROSJEAN M., JOOS F. & KAPLAN J. O. 2008. Mid-to Late Holocene climate change: an overview. *Quaternary Science Reviews* **27**, 1791-1828.
ZEBIAK S. E., ORLOVE B., MUÑOZ Á. G., VAUGHAN C., HANSEN J., TROY T., THOMSON M. C., LUSTIG A. & GARVIN S. 2015. Investigating El Niño‐Southern Oscillation and society relationships. *Wiley Interdisciplinary Reviews: Climate Change* **6**, 17-34.

APPENDIX A: CORE SAMPLING

Core Collection

The 2015 coring expedition to Swallow Lagoon (S 27.49846, E 153.45500) was conducted over two days. On 17 May, the coring platform was assembled and secured in place, then on 18 May two cores were collected and extruded into sample bags. The first core, SL-15/1, was taken from the mid-north side of the lagoon, just beyond the vegetation line, where *L. articulate* stopped growing, (S 27.49856, E 153.45468). The second core, SL-15/2, was taken within the vegetation line, under an overhanging stand of *m. quinquenervia* on the eastern shore (S 27.49884, E 153.45503).

MATERIALS:

- Soft sediment piston corer (internal diameter 80mm)
- Auger poles
- Steel Cable
- Two 3.75 m tin boats
- One 3.25 m tin boat with battery powered propeller
- Three spools of rope
- Four ratchet tie down straps
- Two planks of wood
- Hondex PS-7 Portable Depth Sounder
- Garmin eTrex® 20 GPS
- 1 m collapsible ruler
- Tripod
- Extrusion pallet knife and guide-rings
- Deionised (DI) water rinse bottle
- Plastic zip-lock bags
- Duct Tape

PROCEDURE:

1. The two 3.75m tin boats were taken into the water at the edge of the lagoon and two planks placed across them perpendicular to their length to form a stable platform, leaving a space between the two hulls for the corer. These planks were secured in place using tie down straps with a ratchet mechanism to tighten them. The platform was launched and positioned over the desired core location then secured in place with ropes stretching from the port bow, starboard bow and aft to the respective shores of the lagoon and tied to trees there. The lengths of these ropes were adjusted to change the position of the platform on the lagoon.

Figure 9: The coring platform, constructed from two 3.75 m tin boats sits above the location of core SL/15-1. Photo by J. Greer

2. The GPS reading and depth to lake bottom were measured and recorded above the core location.
3. The piston corer was submerged and allowed to fill with water, then lowered on the end of the auger poles to the depth indicated by the depth sounder so that it was just resting on the lake bed.
4. Pushing down on the auger poles forced the perspex core barrel 1 m into the lake bed while the piston rested on the sediment surface, causing a vacuum to be formed within the tube which helped to recover and keep the sediment in place.

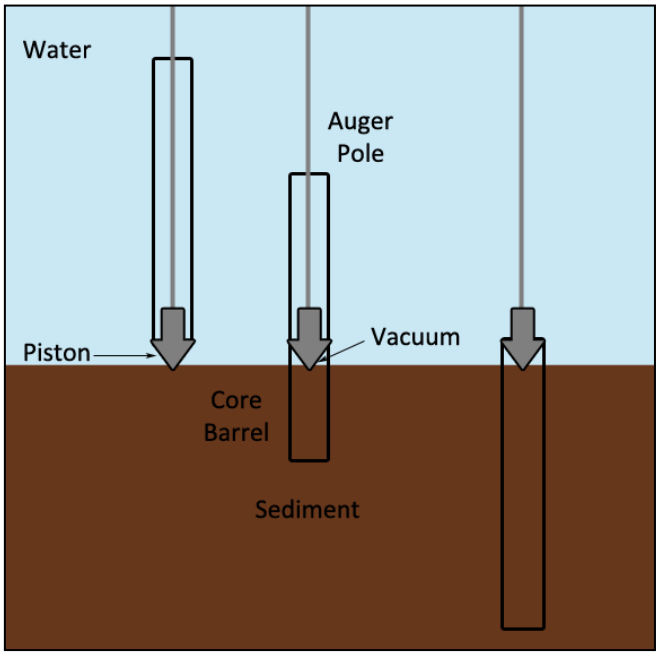

Figure 10: A diagram of the soft sediment piston corer, adapted from Ocean Studies Board and Mapping Science Committee (2004).

5. The corer was then raised to the surface, keeping the steel cable tight to ensure the piston head remained at the top of the perspex tube.
6. Once the bottom of the core was within reach, a rubber puck was inserted into the base of the tube to seal the core in place while the core was raised onto the platform.
7. The auger poles were removed from the coring mechanism and the core length measured and inspected for leaf content.
8. The third boat was used to transfer the core back to shore while keeping it upright and the puck firmly in the base.
9. The perspex tube was secured on a tripod and the piston head removed to expose the top of the core.
10. Using a bundle of auger poles taped together to push up on the puck, the core was extruded from the tube by 1 cm.
11. The top 1 cm was sliced from the core using a pallet knife, pushed through the core between two guide rings. The knife and top ring were then used to place the sample in a zip-lock bag, duct taped closed and labelled.
12. The pallet knife and guide-rings were rinsed with DI water and steps 11 and 12 repeated for the length of the core.

Separating *M. quinquenervia* leaves from lake sediment

After the first 20 samples were collected, a faster approach which only targeted larger leaves was developed to save time. Steps 5, 6 and 9 were removed, and step 7 was amended to only target material that looked like target leaves. Remaining material was washed back into the sample bag using RO water.

MATERIALS:

- 2000 mL glass beaker
- 100 mL glass beaker
- Ashed Al foil
- 0.5 mm sieve
- Pressure Sprayer
- Tweezers
- Spike tool
- Watch glass
- Zeiss Stereoscope with adjustable magnification
- Reverse Osmosis (RO) water rinse bottle
- 50 mL falcon tubes (1/ sample)
- 120 mL plastic containers (2/ sample)
- Solvent rinse bottles: Methanol, Dichloromethane, Hexane, (MeOH, DCM, C_6H_{14})

PROCEDURE:

1. The zip-lock sample bags were opened, half filled with RO water and gently agitated to loosen up the lake sediments.
2. The sample bags were then washed out using the RO water rinse bottle into a 0.5 mL sieve positioned over a large, 2000 mL beaker so that the fine grained material could be collected.
3. The first 500 mL of <0.5 mm fraction was placed aside and left to settle for 2-3 days until the top 400 mL of clear water could be decanted and the remaining 120 mL stored in a plastic container. This was then refrigerated for later study.
4. Using a pressure sprayer filled with tap water, the remaining fine sediment was broken up and washed through the sieve.
5. The remaining material was rinsed with RO water and any large pieces which were obviously not *m. quinquenervia* leaves (sticks, bark, gumnuts etc.) were picked out and placed into a separate 120 mL container set aside for the other material collected.
6. Tap water was then directed from the tap through a plastic tube onto the remaining material to position it near the edge of the sieve for easy retrieval, this was again rinsed with RO water.
7. Using the tweezers and careful rinses with RO water, a batch of material was directed into a watch glass and taken to the stereoscope for leaf picking.

8. Using tweezers and a metal spike tool, the *m. quinquenervia* leaves were identified and separated from the other material and placed into 50 mL falcon tubes to be frozen and then freeze dried.
9. All remaining material >0.5 mm from each batch was emptied into the 100 mL container set aside earlier for other material, also to be frozen and then freeze dried.
10. Steps 8 and 9 were repeated until all the material in the sieve had been collected.
11. The sieve and beaker were washed out with RO water and the sieve given a three solvent rinse of MeOH, DCM and C_6H_{14} between each sample.

Identifying *M. quinquenervia* leaves

Melaleuca quinquenervia leaves and leaf fragments are identifiable due to several features which together provide a distinctive appearance compared to the other leaf matter in the core samples.

- Orange to reddish-brown colouration
- Five veins running parallel to the leaf length
- Thick stem with absence of a central leaf vein
- Pattern of oil glands on the leaf between the veins
- The waxy cuticle can interfere with correct identification in younger samples where it is fully intact but a small part may be removed to reveal the above features. Or the sample may be backlit to reveal the five veins running through the leaf.

APPENDIX B: LABORATORY PROCEEDINGS

Freeze Drying

Once samples were picked, they needed to be freeze dried for storage and isotopic analysis.

MATERIALS:

- Test tube rack
- Freezer set to -16 °C
- Scanvac CoolSafe® freeze drier
- Rotary Pump

PROCEDURE:

1. The rotary pump was switched on so that it could warm up. The freeze drier was turned on at this time so that it could cool down from room temperature. The isolation valve was closed throughout the start-up period.
2. Samples which had fully frozen in the -16 °C freezer were retrieved and placed in a test tube rack. The lids were slightly unscrewed so that water could escape once it sublimed. They were returned to the freezer until needed.
3. Once the freeze drier reached -55 °C, the samples were moved from the freezer and placed in the chamber of the freeze drier.
4. The isolation valve between the rotary pump and the freeze drier was opened and a vacuum was allowed to build up in the chamber.
5. Once the samples were visibly dry, after 2-3 days, the isolation valve was closed and the chamber depressurised.
6. If the lid of the chamber could be removed right away, all the samples were dry. If the chamber had to depressurise fully, one or more still contained water.
7. By feeling the bottom of the tubes, the dry samples could be identified as those which were not cold to the touch. Others were returned to the freeze drier and the isolation valve was opened again for the freeze drying process to resume.
8. Once the chamber was empty of all samples and depressurised, the machines could be switched off, and a bucket placed under the drainage port as it was opened to collect any water collected as it thawed.

Grinding Samples

Dried leaf samples needed to be ground for isotope analysis.

MATERIALS:

- Retsch MM400 ball mill
- 24 sample Retsch milling racks and 3 mm ball bearings
- 2 mL centrifuge tubes
- Ultrasonic bath
- Tweezers, scoops
- Electronic scales (6. sig. figs.)
- Ashed Al foil boats
- Solvent rinse bottles: Methanol, Dichloromethane, Hexane, (MeOH, DCM, C_6H_{14})

PROCEDURE:

1. Scoops and tweezers were washed, and triple rinsed with MeOH, DCM and C_6H_{14}.
2. Ball bearings were submerged in methanol and sonicated in an ultrasonic bath for 15 minutes, and then triple rinsed with Dichloromethane and Hexane.
3. Samples were placed into the milling cups with a large ball bearing, such that the cups were balanced.
4. Samples were emptied into an Al foil boat and weighed into 2 mL centrifuge tubes on the electronic scales. Each sample had 0.005 g weighed out for bulk carbon ^{13}C and 0.120 g (split between two tubes) for cellulose extraction.
5. The samples for bulk carbon ^{13}C were placed into the milling racks, with 2 ball bearings and run at 27 Hz for 30 seconds, leaving the samples finely powdered.
6. The larger samples for cellulose extraction were run with 2 ball bearings at 27 Hz for 60 seconds, until these were also finely powdered.

Weighing Samples for Isotopic Analysis

Target sample weight for carbon was between 0.20 - 2.00 mg. Carbon standards were Glutamic acid (1.00 mg), Triphenylamine (0.50 mg) and Glycine (0.10, 0.20, 0.50, 1.00, 2.00 mg).

MATERIALS:

- Electronic scales (6 sig. figs.)
- Tin boats
- Spatula
- Scoop
- Curved tweezers
- Ceramic tile
- Plastic tray
- Kimwipes
- Solvent rinse bottle: Ethanol (C_2H_6O)
- Glycine
- Glutamic Acid
- Triphenylamine

PROCEDURE:

1. Using curved tweezers to handle them, a metal boat were placed on the electronic scales and the scales zeroed, then it was placed on a ceramic tile to be filled.
2. Using the scoop and spatula, a sample/standard was added to the boat and its weight checked.
3. When the weight was correct, the boat was sealed by crimping the top closed with the tweezers.
4. The boat was then added to a plastic tray with containers corresponding to the spaces on the run sheet, where the sample/standard had its position recorded.
5. Between each sample/standard, the tools and workspace were cleaned with kimwipes and ethanol.

ANSTO Laboratory Experience

Material from ten core sections was taken to the Australian Institute of Nuclear Science and Engineering, The Australian Nuclear Science and Technology Organisation to build up a more detailed age-depth model.

Chemical Pre-treatment

Samples taken for radiocarbon dating needed to be decontaminated using a series of chemical reactions.

MATERIALS:

- Test tube rack
- Electronic scales (6 sig. figs.)
- 50 mL centrifuge tubes
- Spatula
- Tweezers
- Plastic Pipettes
- Grant OLS200 waterbath
- Hydrochloric Acid (2M)
- Sodium Hydroxide (0.5%)
- Rinse bottle: Milli-Q water
- Labec Drying oven
- Glass vials
- Al foil

PROCEDURE:

1. Using electronic scales and tweezers, 0.05 g of dried *m. quinquenervia* was weighed out into 50 mL centrifuge tubes.
2. Using a plastic pipette, the samples were covered with ~ 7.5 mL of 2M HCl, ensuring that each sample was fully submerged.
3. Once submerged in HCl, the samples were heated in a waterbath set to 60°C for 2 hours.
4. After 2 hours, the HCl was removed via a dedicated plastic pipette for each sample. These pipettes were then rinsed with Milli-Q water.
5. Using the rinse bottle, 50 mL of Milli-Q water was added to each sample. The water was then removed via the dedicated plastic pipette for each sample. These pipettes were then rinsed with Milli-Q water.
6. Step 5. was repeated for a total of three rinses.
7. Using a plastic pipette, the samples were covered with ~ 7.5 mL of 0.5% NaOH, ensuring that each sample was fully submerged.
8. Once submerged in NaOH, the samples were heated in a waterbath set to 60°C for 2 hours. Checking after 1 hour to ensure the samples were not being dissolved by the NaOH.

9. After 2 hours, the NaOH was removed via the dedicated plastic pipette for each sample. These pipettes were then rinsed with Milli-Q water.
10. Using the rinse bottle, 25 mL of Milli-Q water was added to each sample. The water was then removed via the dedicated plastic pipette for each sample. These pipettes were then rinsed with Milli-Q water.
11. Steps 7-10. were repeated for a total of 3 washes with 0.5% NaOH.
12. Using the rinse bottle, 50 mL of Milli-Q water was added to each sample. The water was then removed via the dedicated plastic pipette for each sample. These pipettes were then rinsed with Milli-Q water.
13. Step 12. was repeated for a total of two rinses.
14. Using a plastic pipette, the samples were covered with ~ 7.5 mL of 1% NaOH, ensuring that each sample was fully submerged.
15. Once submerged in NaOH, the samples were heated in a waterbath set to 60°C for 2 hours. Checking after 1 hour to observe the progress of the reaction.
16. After 2 hours, the NaOH was removed via the dedicated plastic pipette for each sample. These pipettes were then rinsed with Milli-Q water.
17. Using the rinse bottle, 25 mL of Milli-Q water was added to each sample. The water was then removed via the dedicated plastic pipette for each sample. These pipettes were then rinsed with Milli-Q water.
18. If solution was not clear, steps 14-17 were repeated.
19. Once the solution was clear, using the rinse bottle, 50 mL of Milli-Q water was added to each sample. The water was then removed via the dedicated plastic pipette for each sample. These pipettes were then rinsed with Milli-Q water.
20. Step 19. was repeated for a total of three rinses.
21. Using a plastic pipette, the samples were covered with ~ 7.5 mL of 2M HCl, ensuring that each sample was fully submerged.
22. Once submerged in HCl, the samples were left to sit at room temperature for 2 hours.
23. After 2 hours, the HCl was removed via a dedicated plastic pipette for each sample. These pipettes were then rinsed with Milli-Q water.
24. Using the rinse bottle, 50 mL of Milli-Q water was added to each sample. The water was then removed via the dedicated plastic pipette for each sample. These pipettes were then rinsed with Milli-Q water.
25. Step 25. was repeated for a total of three rinses.
26. A glass vial was labelled for each sample and weighed on the electronic scales.
27. Each sample was transferred into its corresponding vial using a spatula and the vial loosely capped with Al foil.
28. The samples were then dried overnight in a drying oven set to 60°C.

Sample Processing

Dried samples having been pre-treated to remove contaminants needed to be converted to CO_2 and then to graphite before they could be dated.

MATERIALS:

- Electronic scales (6 sig. figs.)
- Spatula
- Tweezers
- Quartz tubes
- Copper oxide (CuO)
- Silver wire (Ag)
- Copper wire (Cu)
- Plastic film
- Vacuum line
- Furnace

PROCEDURE:

1. Two spatula scoops full of CuO were added into quartz tubes and its weight torn on the electronic scales.
2. Using a separate pair of tweezers for each sample, small pieces of sample material were broken off and weighed into the quartz tube until 2 mg of sample was in the tube.
3. Two more spatula scoops of CuO were poured into the tube, making sure the spatula did not come into contact with the quartz tube after the sample had touched it.
4. Using tweezers, one Ag and one Cu wire were placed into the tube.
5. The tube was temporarily sealed with a plastic film while it was transported to the vacuum line.
6. The sample was placed under vacuum for 30 minutes.
7. Once the samples were under vacuum, the quartz tube was sealed with a blowtorch and broken off from the vacuum line.
8. The sealed samples were placed in a furnace set to 900°C overnight.
9. After combustion, tubes containing gaseous samples were scored to enable them to be broken, then taken to the vacuum line and sealed inside.
10. Once under a vacuum, the sample gas was released from the tube by breaking the quartz open.
11. H_2O was precipitated out in a trap chilled by a dry ice slurry before the gas was allowed to pass to the next stage of the line.
12. CO_2 was precipitated out in a trap chilled by liquid nitrogen and the remaining gas allowed to exit the line.
13. CO_2 was passed through the rest of the line and collected in a glass tube with a stopcock to be taken for graphitisation.

14. In a dedicated vacuum line, sample CO_2 was transferred into a cold finger chilled with liquid nitrogen.
15. The system was sealed and the CO_2 was allowed to thaw, then pressure within the line was measured to calculate the amount of CO_2 present.
16. The CO_2 was frozen again and the line opened for the introduction of H_2 gas, until ratio of $2H_2$:CO_2 was achieved.
17. Then the system was sealed and the CO_2 was reacted with H_2 gas in the presence of an Fe catalyst at 600°C, and H_2O produced by the reaction was collected in a tube chilled to -36°C.
18. Graphite sample was weighed and loaded into a cathode, which could be taken for AMS analysis.

AMS dating at Waikato Radiocarbon Dating Laboratory

Using electronic scales, 0.06 g of dried *m. quinquenervia* from three different depths within the core were weighed out into 10 mL centrifuge tubes. Samples were selected from sections which had yielded large quantities of leaf matter. This material was sent for Accelerator Mass Spectrometry (AMS) radiocarbon dating at Waikato Radiocarbon Dating Laboratory, University of Waikato, New Zealand.

The AMS technique employed by Waikato Radiocarbon Dating Laboratory is similar to that detailed in ANSTO Laboratory Experience. A slight difference in temperatures and reagents used during sample processing as follows:

Organic samples are converted to CO_2 by oxidation using CuO at 800^{o}C rather than 900^{o}C. The CO_2 is purified in the presence of silver wire, but not copper wire to absorb any SOx and NOx that is produced. The CO_2 is then reduced to graphite with H_2 at 550^{o}C, rather than 600^{o}C using an iron catalyst.
Pressed graphite sample is sent to the Keck Radiocarbon Dating Laboratory at the University of California, Irvine and the Center for Applied Isotope Studies, University of Georgia for analysis.

APPENDIX C: RESULTS TABLES AND SUPPLEMENTARY FIGURES

Table of Isotopic Results

Table 6: Sample depths are shown with the corresponding model age. The dry leaf yield for each sample is shown, along with EA-IRMS %C and $\delta^{13}C$ results. An early diagenesis correction of +1 ‰ is applied to $\delta^{13}C$ before conversion to ΔC.

Sample ID	Base Depth (cm)	Model Age (CE)	Dry leaf mass (mg)	%C	$\delta^{13}C$ (‰)	$\delta^{13}C$+1 (‰)
SL-15/2-1	1	2013	55.9	57.62	-32.03	-31.03
SL-15/2-2	2	2006	3.2	58.89	-31.53	-30.53
SL-15/2-3	3	2004	286.5	55.69	-31.31	-30.31
SL-15/2-4	4	2003	450.8	52.05	-31.39	-30.39
SL-15/2-5	5	2001	127.9	53.97	-31.33	-30.33
SL-15/2-6	6	1999	131.5	53.90	-31.33	-30.33
SL-15/2-7	7	1998	75.6	56.67	-31.20	-30.20
SL-15/2-8	8	1997	240.2	50.70	-31.04	-30.04
SL-15/2-9	9	1997	152.4	53.79	-31.57	-30.57
SL-15/2-10	10	1995	51.4	51.71	-30.61	-29.61
SL-15/2-11	11	1995	70.2	53.63	-30.93	-29.93
SL-15/2-12	12	1995	72.1	57.52	-32.12	-31.12
SL-15/2-13	13	1994	131.9	55.25	-30.81	-29.81
SL-15/2-14	14	1994	111.3	49.84	-30.95	-29.95
SL-15/2-15	15	1993	191.7	56.06	-30.49	-29.49
SL-15/2-16	16	1973	166.4	58.37	-31.37	-30.37
SL-15/2-17	17	1958	109.9	49.39	-30.98	-29.98
SL-15/2-18	18	1950	67.8	55.15	-30.82	-29.82
SL-15/2-19	19	1941	52.9	57.18	-31.17	-30.17
SL-15/2-20	20	1931	61.9	52.68	-30.39	-29.39
SL-15/2-21	21	1911	141.0	50.72	-31.73	-30.73
SL-15/2-22	22	1888	111.6	63.75	-30.93	-29.93
SL-15/2-23	23	1877	201.9	58.23	-29.02	-28.02
SL-15/2-24	24	1871	10.2	53.18	-31.10	-30.10
SL-15/2-25	25	1864	10.1	49.14	-30.42	-29.42
SL-15/2-26	26	1856	92.7	56.19	-30.54	-29.54
SL-15/2-27	27	1847	23.5	54.43	-29.72	-28.72
SL-15/2-28	28	1838	40.3	56.37	-31.47	-30.47
SL-15/2-29	29	1829	40.6	56.50	-31.58	-30.58
SL-15/2-30	30	1819	107.9	57.23	-31.20	-30.20
SL-15/2-31	31	1809	48.9	57.30	-29.68	-28.68
SL-15/2-32	32	1799	50.7	53.83	-30.96	-29.96
SL-15/2-33	33	1790	46.9	58.55	-29.36	-28.36
SL-15/2-34	34	1780	96.1	54.23	-29.38	-28.38
SL-15/2-35	35	1771	72.1	58.01	-29.93	-28.93

Sample ID	Base Depth (cm)	Model Age (CE)	Dry leaf mass (mg)	%C	$\delta^{13}C$ (‰)	$\delta^{13}C+1$ (‰)
SL-15/2-36	36	1762	38.6	55.18	-31.15	-30.15
SL-15/2-37	37	1753	74.0	56.46	-29.78	-28.78
SL-15/2-38	38	1745	101.9	51.46	-30.79	-29.79
SL-15/2-39	39	1737	42.6	56.16	-29.01	-28.01
SL-15/2-40	40	1724	25.0	51.77	-31.21	-30.21
SL-15/2-41	41	1683	59.4	62.76	-30.41	-29.41
SL-15/2-42	42	1669	40.1	53.97	-29.76	-28.76
SL-15/2-43	43	1658	6.1	54.33	-29.97	-28.97
SL-15/2-44	44	1638	14.6	57.19	-30.47	-29.47
SL-15/2-45	45	1610	57.1	63.12	-30.34	-29.34
SL-15/2-46	46	1579	26.0	52.81	-28.45	-27.45
SL-15/2-47	47	1545	29.2	53.29	-29.88	-28.88
SL-15/2-48	48	1510	52.1	61.07	-30.24	-29.24
SL-15/2-49	49	1475	12.1	60.04	-29.83	-28.83
SL-15/2-50	50	1439	24.3	54.46	-30.04	-29.04
SL-15/2-51	51	1404	63.0	60.13	-30.22	-29.22
SL-15/2-52	52	1369	44.0	64.53	-29.89	-28.89
SL-15/2-53	53	1335	84.8	64.48	-30.55	-29.55
SL-15/2-54	54	1301	38.6	54.25	-29.29	-28.29
SL-15/2-55	55	1271	79.1	58.40	-29.75	-28.75
SL-15/2-56	56	1245	62.7	51.50	-29.41	-28.41
SL-15/2-57	57	1224	145.2	59.00	-30.12	-29.12
SL-15/2-58	58	1209	135.1	61.86	-29.79	-28.79
SL-15/2-59	59	1191	87.6	61.74	-30.26	-29.26
SL-15/2-60	60	1172	71.0	71.27	-30.26	-29.26
SL-15/2-61	61	1148	99.3	58.33	-30.64	-29.64
SL-15/2-62	62	1129	80.8	54.62	-30.77	-29.77
SL-15/2-63	63	1107	94.9	56.78	-30.61	-29.61
SL-15/2-64	64	1092	90.9	58.05	-31.22	-30.22
SL-15/2-65	65	1078	147.5	61.82	-29.94	-28.94
SL-15/2-66	66	1054	209.7	59.12	-30.73	-29.73
SL-15/2-67	67	1026	310.7	59.85	-30.30	-29.30
SL-15/2-68	68	984	162.2	57.70	-30.29	-29.29
SL-15/2-69	69	956	168.2	59.95	-29.50	-28.50
SL-15/2-70	70	934	155.4	57.75	-29.10	-28.10
SL-15/2-71	71	913	219.0	62.67	-29.54	-28.54
SL-15/2-72	72	896	517.5	59.43	-30.00	-29.00
SL-15/2-73	73	881	340.5	67.44	-30.17	-29.17
SL-15/2-74	74	864	487.7	59.29	-28.99	-27.99
SL-15/2-75	75	846	390.5	52.93	-29.24	-28.24
SL-15/2-76	76	827	535.9	56.66	-28.82	-27.82
SL-15/2-77	77	808	350.6	60.46	-29.43	-28.43

Sample ID	Base Depth (cm)	Model Age (CE)	Dry leaf mass (mg)	%C	$\delta^{13}C$ (‰)	$\delta^{13}C+1$ (‰)
SL-15/2-78	78	789	141.1	57.12	-29.83	-28.83
SL-15/2-79	79	772	64.9	58.91	-29.39	-28.39
SL-15/2-80	80	757	128.6	55.65	-31.25	-30.25
SL-15/2-81	81	742	174.6	56.31	-29.88	-28.88
SL-15/2-82	82	723	181.7	55.56	-29.44	-28.44
SL-15/2-83	83	703	196.1	56.71	-29.66	-28.66
SL-15/2-84	84	680	334.5	55.38	-31.06	-30.06
SL-15/2-85	85	667	264.2	55.15	-29.19	-28.19
SL-15/2-86	86	647	291.7	58.52	-30.17	-29.17
SL-15/2-87	87	612	105.0	56.65	-29.62	-28.62
SL-15/2-88	88	579	23.8	54.21	-30.11	-29.11
SL-15/2-89	89	555	128.8	57.76	-29.67	-28.67
SL-15/2-90	90	533	241.2	55.93	-29.24	-28.24
SL-15/2-91	91	514	71.9	57.11	-29.91	-28.91

Rainfall Reconstruction

Table 7: Sample depths with corresponding modeled age. The values for atmospheric δ13C and *p*CO2 used to calculate Δ are provided, as well as the measured and predicted Δ, and Δ anomaly with the final rainfall reconstruction.

Sample ID	Model Age (CE)	atmos. $\delta^{13}C$ (‰)	atmos. pCO_2 (‰)	Δ (‰)	Pred. Δ (‰)	Δ anomaly (‰)	Rainfall (mm)
SL-15/2-1	2013	-8.46	392.8	23.29	21.38	1.91	1230
SL-15/2-2	2006	-8.27	378.7	22.97	21.19	1.77	1200
SL-15/2-3	2004	-8.09	374.8	22.92	21.14	1.78	1201
SL-15/2-4	2003	-8.09	372.9	23.00	21.12	1.88	1224
SL-15/2-5	2001	-7.99	368.5	23.03	21.06	1.97	1243
SL-15/2-6	1999	-7.98	365.7	23.05	21.02	2.03	1255
SL-15/2-7	1998	-7.96	363.7	22.93	20.99	1.94	1236
SL-15/2-8	1997	-7.90	361.3	22.83	20.96	1.87	1221
SL-15/2-9	1997	-7.90	361.3	23.38	20.96	2.42	1340
SL-15/2-10	1995	-7.89	359.9	22.37	20.94	1.44	1128
SL-15/2-11	1995	-7.89	358.3	22.72	20.92	1.81	1208
SL-15/2-12	1995	-7.89	358.3	23.98	20.92	3.06	1478
SL-15/2-13	1994	-7.82	356.4	22.67	20.89	1.78	1201
SL-15/2-14	1994	-7.82	356.4	22.82	20.89	1.93	1234
SL-15/2-15	1993	-7.79	354.9	22.35	20.87	1.49	1139
SL-15/2-16	1973	-7.28	327.2	23.82	20.45	3.37	1543
SL-15/2-17	1958	-6.93	315.4	23.76	20.25	3.51	1574

Sample ID	Model Age (CE)	atmos. $\delta^{13}C$ (‰)	atmos. pCO_2 (‰)	Δ (‰)	Pred. Δ (‰)	Δ anomaly (‰)	Rainfall (mm)
SL-15/2-18	1950	-6.88	312.3	23.65	20.20	3.45	1561
SL-15/2-19	1941	-6.78	309.7	24.11	20.16	3.96	1670
SL-15/2-20	1931	-6.73	306.0	23.35	20.09	3.26	1519
SL-15/2-21	1911	-6.68	300.7	24.82	20.00	4.82	1855
SL-15/2-22	1888	-6.56	294.1	24.09	19.88	4.22	1725
SL-15/2-23	1877	-6.54	292.1	22.10	19.84	2.26	1304
SL-15/2-24	1871	-6.48	291.0	24.35	19.82	4.53	1792
SL-15/2-25	1864	-6.48	289.7	23.64	19.79	3.85	1646
SL-15/2-26	1856	-6.46	288.2	23.78	19.77	4.01	1682
SL-15/2-27	1847	-6.41	286.5	22.97	19.73	3.24	1515
SL-15/2-28	1838	-6.49	285.8	24.73	19.72	5.01	1895
SL-15/2-29	1829	-6.50	285.3	24.84	19.71	5.13	1921
SL-15/2-30	1819	-6.46	284.8	24.48	19.70	4.78	1846
SL-15/2-31	1809	-6.40	284.3	22.94	19.69	3.25	1517
SL-15/2-32	1799	-6.35	283.8	24.34	19.68	4.66	1820
SL-15/2-33	1790	-6.32	281.1	22.68	19.63	3.05	1475
SL-15/2-34	1780	-6.31	279.9	22.72	19.61	3.11	1488
SL-15/2-35	1771	-6.30	278.5	23.31	19.58	3.73	1621
SL-15/2-36	1762	-6.28	277.0	24.61	19.55	5.06	1906
SL-15/2-37	1753	-6.29	277.0	23.17	19.55	3.62	1596
SL-15/2-38	1745	-6.36	276.9	24.14	19.55	4.60	1807
SL-15/2-39	1737	-6.30	277.1	22.34	19.55	2.78	1417
SL-15/2-40	1724	-6.31	277.4	24.64	19.56	5.09	1912
SL-15/2-41	1683	-6.26	276.1	23.86	19.53	4.33	1750
SL-15/2-42	1669	-6.26	276.3	23.16	19.54	3.63	1599
SL-15/2-43	1658	-6.27	276.8	23.38	19.54	3.84	1643
SL-15/2-44	1638	-6.28	276.6	23.90	19.54	4.35	1755
SL-15/2-45	1610	-6.30	274.7	23.74	19.50	4.23	1729
SL-15/2-46	1579	-6.31	280.4	21.73	19.62	2.11	1273
SL-15/2-47	1545	-6.32	282.8	23.23	19.66	3.57	1587
SL-15/2-48	1510	-6.33	282.7	23.60	19.66	3.94	1665
SL-15/2-49	1475	-6.34	280.4	23.16	19.62	3.54	1580
SL-15/2-50	1439	-6.35	281.5	23.37	19.64	3.73	1621
SL-15/2-51	1404	-6.36	280.6	23.56	19.62	3.94	1665
SL-15/2-52	1369	-6.36	281.2	23.20	19.63	3.56	1585
SL-15/2-53	1335	-6.36	283.0	23.89	19.67	4.23	1728
SL-15/2-54	1301	-6.37	282.9	22.55	19.66	2.89	1440
SL-15/2-55	1271	-6.37	282.2	23.04	19.65	3.39	1548
SL-15/2-56	1245	-6.36	281.7	22.69	19.64	3.05	1475
SL-15/2-57	1224	-6.36	282.7	23.44	19.66	3.78	1632
SL-15/2-58	1209	-6.36	283.3	23.10	19.67	3.43	1555
SL-15/2-59	1191	-6.36	283.9	23.59	19.68	3.90	1658

Sample ID	Model Age (CE)	atmos. $\delta^{13}C$ (‰)	atmos. pCO_2 (‰)	Δ (‰)	Pred. Δ (‰)	Δ anomaly (‰)	Rainfall (mm)
SL-15/2-60	1172	-6.37	283.9	23.57	19.68	3.89	1655
SL-15/2-61	1148	-6.38	283.8	23.96	19.68	4.28	1739
SL-15/2-62	1129	-6.39	283.3	24.10	19.67	4.42	1770
SL-15/2-63	1107	-6.40	282.7	23.92	19.66	4.26	1734
SL-15/2-64	1092	-6.41	282.2	24.56	19.65	4.90	1873
SL-15/2-65	1078	-6.41	281.6	23.20	19.64	3.55	1583
SL-15/2-66	1054	-6.42	280.6	24.02	19.62	4.40	1765
SL-15/2-67	1026	-6.43	279.9	23.56	19.61	3.95	1669
SL-15/2-68	984	-6.41	277.2	23.57	19.55	4.01	1682
SL-15/2-69	956	-6.37	276.7	22.78	19.54	3.24	1515
SL-15/2-70	934	-6.34	277.3	22.39	19.55	2.83	1428
SL-15/2-71	913	-6.31	277.9	22.88	19.57	3.32	1532
SL-15/2-72	896	-6.45	278.3	23.23	19.58	3.65	1604
SL-15/2-73	881	-6.45	278.7	23.41	19.58	3.82	1641
SL-15/2-74	864	-6.44	279.1	22.17	19.59	2.58	1373
SL-15/2-75	846	-6.44	278.8	22.44	19.58	2.85	1432
SL-15/2-76	827	-6.44	278.5	21.99	19.58	2.42	1338
SL-15/2-77	808	-6.43	278.2	22.64	19.57	3.07	1479
SL-15/2-78	789	-6.43	277.9	23.07	19.57	3.50	1571
SL-15/2-79	772	-6.43	277.7	22.60	19.56	3.03	1471
SL-15/2-80	757	-6.42	277.9	24.57	19.57	5.01	1895
SL-15/2-81	742	-6.42	278.1	23.12	19.57	3.55	1583
SL-15/2-82	723	-6.42	278.4	22.67	19.58	3.09	1483
SL-15/2-83	703	-6.41	278.7	22.90	19.58	3.32	1532
SL-15/2-84	680	-6.41	278.5	24.38	19.58	4.80	1851
SL-15/2-85	667	-6.41	278.3	22.41	19.58	2.84	1429
SL-15/2-86	647	-6.40	278.1	23.45	19.57	3.88	1652
SL-15/2-87	612	-6.40	277.7	22.87	19.56	3.31	1531
SL-15/2-88	579	-6.39	277.5	23.40	19.56	3.84	1644
SL-15/2-89	555	-6.39	277.9	22.94	19.57	3.38	1545
SL-15/2-90	533	-6.38	278.3	22.49	19.57	2.92	1446
SL-15/2-91	514	-6.38	278.6	23.20	19.58	3.62	1598

Historical Rainfall Correlation

The raw Δ values and the Δ anomaly for the historical period were compared to time-averaged precipitation records (refer to appendix). The precipitation values were modified by averaging annual records from all years covered by the sample, derived from the age-depth model. Annual precipitation from SILO and BOM datasets was also averaged over the time interval that corresponded to each one centimetre sample. Although the best relationship was found with between Δ anomaly and the data from SILO, no significant correlation was found between raw Δ or Δ anomaly and either SILO or BOM precipitation records (Figure 11).

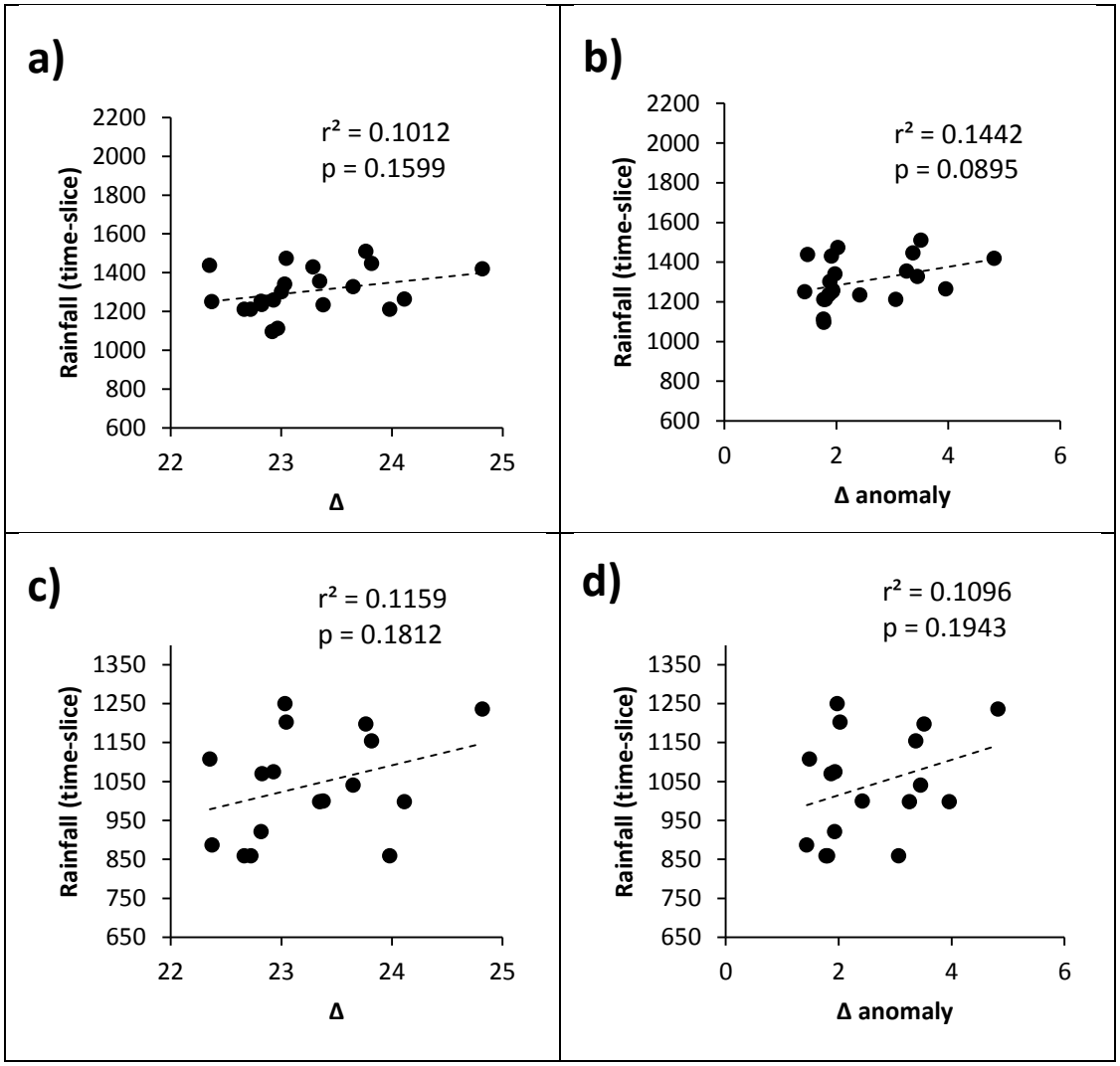

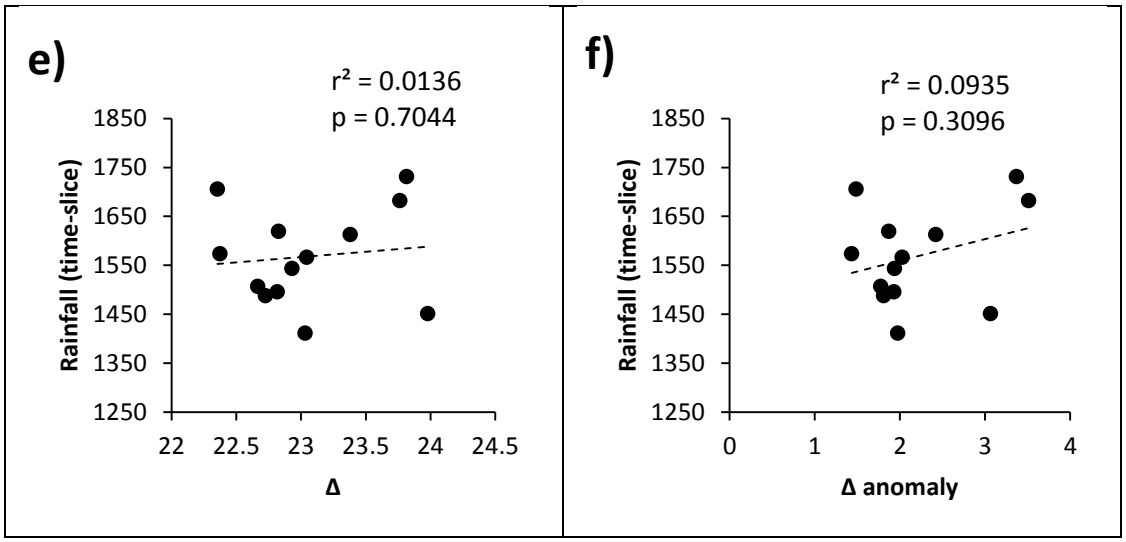

Figure 11: Attempted linear regressions through the historical period (1911–2013) *M. quinquenervia* Δ (‰) compared to average annual rainfall averaged across each sample interval with a three year lag are shown below. The dashed lines indicate that the regressions are not significant (p > 0.05). SILO data collated by the Queensland Government DSITI are plotted a) directly against Δ, and b) against Δ anomaly. Toowong Bowls Club Station records from the Australian Government Bureau of Meteorology are plotted c) directly against Δ, and d) against Δ anomaly. Point Lookout Station records from the Australian Government Bureau of Meteorology are plotted e) directly against Δ, and f) against Δ anomaly.